POLITECNICO DI TORINO
Repository ISTITUZIONALE

Defining the influence area of uplift and subsidence from underground gas storage in anticline structural traps: Insights from InSAR cross-correlation

Original
Defining the influence area of uplift and subsidence from underground gas storage in anticline structural traps: Insights from InSAR cross-correlation / Codegone, G., Benetatos, C., Uttini, A., Rucci, A., Fiaschi, S., Mantegazzi, A., Coti, C.. - In: GONDWANA RESEARCH. - ISSN 1342-937X. - ELETTRONICO. - 143:(2025), pp. 185-198. [10.1016/j.gr.2025.03.018]

Availability:
This version is available at: 11583/2999547 since: 2025-05-05T15:24:50Z

Publisher:
Elsevier

Published
DOI:10.1016/j.gr.2025.03.018

Terms of use:

This article is made available under terms and conditions as specified in the corresponding bibliographic description in the repository

Publisher copyright
Elsevier postprint/Author's Accepted Manuscript

© 2025. This manuscript version is made available under the CC-BY-NC-ND 4.0 license http://creativecommons.org/licenses/by-nc-nd/4.0/.The final authenticated version is available online at: http://dx.doi.org/10.1016/j.gr.2025.03.018

(Article begins on next page)

09 November 2026

Defining the influence area of uplift and subsidence from Underground Gas Storage in anticline structural traps: insights from InSAR cross-correlation

Codegone, G.[1*], Benetatos, C.[2], Uttini, A.[3], Rucci, A.[3], Fiaschi, S.[4], Mantegazzi, A.[1], Coti, C.[1]

[1] Stogit Division, Snam S.p.A., Piazza Santa Barbara 7, 20097 San Donato Milanese, Italy

[2] Department of Environment, Land and Infrastructure Engineering, Faculty of Engineering, Politecnico di Torino, Corso Duca degli Abruzzi 24, 10129 Torino, Italy

[3] TRE ALTAMIRA, Ripa di Porta Ticinese, 79, 20143 Milano, Italy

[4] TRE ALTAMIRA, 475 W Georgia St, V6B 4M9, Vancouver, BC, Canada

[*] **Corresponding Author:**

Dr. Giulia Codegone

E-mail address: g.codegone@gmail.com

Submitted to:

Gondwana Research (Research paper)

Abstract

We investigate the relationship between Underground Gas Storage (UGS) operations and ground deformation of three UGS fields in the Po Plain basin, Italy, hosted in Pliocene clastic deposits within anticline structural traps. Sentinel-1 InSAR data from 2015 to 2021 were analyzed to quantify seasonal uplift and subsidence patterns associated with the cyclic injection and withdrawal of gas. The methodology evaluates correlations between UGS activity and the seasonal amplitude of vertical displacement using cross-correlation parameters R and K, which measure the shape (R) and scale (K) similarity between vertical displacement time series and gas volume fluctuations. Results show that, with the UGS injection/withdrawal plan implemented until 2021, seasonal displacement peaks occur within gas field boundaries and diminish outward. Along the major axis of the anticline traps, UGS-related vertical displacements cease before reaching the field boundary, while transversally, they extend up to approximately 0.5 km beyond. Frequency distributions of seasonal amplitude, R and K values were used to define threshold values for R and K, enabling a quantitative identification of the effective UGS influence area, with GNSS data providing additional constraints. Our findings highlight the influence of structural trap geometry and bounding faults in shaping surface subsidence and uplift patterns. These findings underscore the need for advanced monitoring technologies and a comprehensive understanding of subsurface geology to an effective management of UGS operations. As global demand for gas storage increases, integrating geomechanical modeling with ground deformation monitoring will enhance risk assessment, ensure operational safety, and optimize gas storage strategies. The proposed methodology provides valuable insights for monitoring induced ground deformation, offering a framework for sustainable and effective UGS management.

Keywords: InSAR; Underground gas storage; anticline traps; cross-correlation analysis; subsidence monitoring.

1. Introduction

The Po Plain basin in northern Italy is one of the most densely populated regions in Europe and a crucial area for industrial and agricultural activities. Its geological evolution led to the formation of numerous hydrocarbons fields (primarily gas), which have been exploited since the mid-20th century. Since the 1960s, 13 depleted gas fields in the Po Plain have been converted to underground gas storage (UGS) facilities, with others currently under evaluation for future conversion to methane, CO2 or H2 storage. In recent years, the global gas storage capacity has increased due to geopolitical crises that have highlighted the importance of UGS in energy security. UGS systems provide flexibility and help maintain strategic energy reserves. However, the increase in storage capacity requires rigorous safety measures and effective management of the underground resources.

In Italy, public interest in the impact of underground industrial activities on the population and natural environment has grown over the last decade. This awareness gave a great impulse to regulate the monitoring of micro-seismicity, ground deformation, and pore pressure, with the goal of mitigating potential natural and anthropogenic risks (e.g. Dialuce et al., 2014; Braun et al., 2020). Advances in monitoring anthropogenic ground deformations induced by underground activities have been primarily achieved through two complementary technologies: the Interferometric Synthetic Aperture Radar (InSAR) and the Global Navigation Satellite System (GNSS) (e.g. Bertoni et al., 1995; Carminati and Martinelli, 2002; Cenni et al., 2013; Dacome et al., 2015; Codegone et al., 2016; Benetatos et al., 2017; Giani et al., 2017; ARPAE, 2018; Benetatos et al., 2020; Bitelli et al., 2020; Palano et al., 2020; Severi et al., 2020, 2021; Antoncecchi et al., 2021; Calabrese et al., 2021). InSAR enables monitoring over large areas, providing relative measurements of vertical and east-west (E-W) planar movements, while GNSS offers punctual and absolute measurements of vertical, east-west (E-W) and north-south (N-S) planar movements.

UGS operations typically induce cyclical surface oscillations (uplift/subsidence) as a result of seasonal gas injection and withdrawal. The magnitude, extent, and timing of these phenomena depend on numerous factors, including the volume of the injected/withdrawn gas and the associated pressure variation, the presence and properties of surrounding aquifers, the depth, geometry, volume, and petrophysical and geomechanical characteristics of the reservoir and surrounding formations (e.g., Fjær et al., 2008; Benetatos et al., 2020). In a graphical representation vertical displacement vs time, these UGS-related ground oscillations form a “sinusoidal signal” superimposed on background noise characterizing the undisturbed areas. Background noise may include effects from groundwater production, thermal and meteoric phenomena, sediment compaction due to urban settlements, and natural geological processes. Advanced data acquisition

and interpretation techniques are, therefore, required to ensure accurate and high-quality ground displacement monitoring.

Geomechanical models have become essential tools in standard monitoring programs for underground activities in Italy (e.g. Teatini et al., 2006, 2011; Settari et al., 2008; Dialuce et al., 2014; Gambolati and Teatini, 2015; Braun et al., 2020). These models simulate the poro-mechanical processes associated with reservoir pressure changes and their effects on local stress field, which may result in surface uplift and subsidence. The development of geomechanical modelling involves constructing a 3D geological model that integrates geological and geophysical data for an area larger than the reservoir to capture regional and reservoir-scale geological complexities. The size of the 3D grid is designated to properly describe both the reservoir and the surrounding rock volume while ensuring undisturbed boundary conditions. These models are populated with rock mechanical properties to allow simulations that estimate the responses to pressure changes during storage operations. InSAR data are used to calibrate geomechanical parameters, ensuring a suitable match between the simulated and observed ground movements. Once calibrated, the models are used to predict the magnitude and extend of seasonal uplift and subsidence. Vertical ground movements due to subsurface storage operations are generally proportional to the volume of working gas and reservoir pressure changes, with higher values occurring above the reservoir and decreasing radially, suggesting a strong correlation between surface deformation patterns and subsurface geological features (e.g. Castelletto et al., 2010; Teatini et al., 2011; Ferronato et al., 2013; Codegone et al., 2016; Benetatos et al., 2017; Wang et al., 2021; Fibbi et al., 2023).

This study presents results from InSAR data analysis aimed at defining the influence area of the seasonal uplift and subsidence linked to UGS activities at three operative fields in the Po Plain (hereafter referred to as Fields 1, 2 and 3). These fields were selected for their comparable geological characteristics, including trap type (anticline), reservoir lithology, depth, geometry, and overburden stratigraphy. This approach enables a consistent analytical method and a systematic analysis of ground displacements distribution relative to geological features. The methodology characterizes InSAR signal in the three monitored areas in terms of seasonal amplitude and R-K parameters for the vertical component of ground displacement. The present study does not account for the horizontal (E-W planar) seasonal displacements, as these are much lower than the measured vertical displacements (the maximum horizontal seasonal amplitude is about 1/2 than the vertical one). The background noise was characterized in the outermost part of the monitored areas, far enough from the UGS fields to ensure that the measurement points on the ground surfaces were unaffected by UGS-related seasonal oscillations. Threshold values for the R and K parameters were defined so to identify the parts of the InSAR signal that exceed the background noise, effectively attributing them to the UGS. This analytical method can improve modeling accuracy for UGS sites

by providing a more precise delineation of uplift and subsidence areas, thereby improving the calibration of geomechanical parameters. It also enhances our understanding of the UGS-induced variations in the local stress field and their propagation to the surface, leading to more accurate simulations.

2. Geological background

The Po Plain basin extends approximately east to west, from the Western Alps to the Northern Adriatic Sea, and is bounded by two fold-and-thrust belts with opposite vergence: the south-verging Southern Alps, to the north, and the north-northeast-verging Northern Apennines, to the south (e.g. Pieri and Groppi, 1981; Doglioni, 1993; Carminati et al., 2003; Fantoni et al., 2004; Fantoni and Franciosi, 2009; 2010; Balestro et al., 2022). The basin represents the shared foredeep-foreland of these two belts, formed in the context of convergence and continental collision between the Adria microplate and Eurasia (e.g., Dercourt et al., 1986; Fantoni and Franciosi, 2010; Turrini et al., 2016; Irace et al., 2024).

The Cenozoic evolution of the area was primarily controlled by the north-northeastward migration of the Northern Apennine fold-and-thrust belt, which led to the formation of the Po Plain as a foredeep basin. The outer part of the Northern Apennines was structured in the Po Plain subsurface forming three main arcuate thrust systems that are known as the Monferrato, Emilia and Ferrara fold systems (e.g., Pieri and Groppi, 1981; Boccaletti et al., 2011; Festa et al., 2013, 2015; Toscani et al., 2014) (Fig. 1a). During the post-collisional phases, the Southern Alps developed through the back-thrusting of the Alpine chain. The buried south-verging fold-and-thrust belt faces the Northern Apennines in the Po Plain subsurface (e.g., Picotti et al., 1995): the outer tectonic fronts of the Northern Apennines and Southern Alps interact along a deeper, east-west oriented residual foreland (e.g., Fantoni et al., 2004; Scardia et al., 2015) (Fig. 1b).

The structural and stratigraphic architecture of the Po Plain subsurface has been largely studied, described, and explored over the last 40 years, due to its strategic relevance for the natural gas research and exploitation, through seismic reflection lines and deep well data (e.g., Pieri and Groppi, 1981; Casero et al., 2004; Fantoni and Franciosi, 2010; Ghielmi et al., 2010, 2013; Toscani et al., 2014; Turrini et al., 2016; Amadori et al., 2017, 2018, 2019). The main target for gas exploration has been the Plio-Pleistocene syn-tectonic clastic sequences.

At a regional scale, the base of the Pliocene sequence records an abrupt marine transgression over the Northern Apennine foreland, which led the widespread deposition of the marine clays of the

Santerno Formation (Agip, 1982, Ghielmi et al., 2010). Meanwhile, coarse-grained to sand-rich turbidites accumulated in the foredeep areas (Caviaga Formation; Agip, 1982). The coarse-grained turbiditic levels of the Caviaga Formation host the clastic reservoir of the UGS Field 2. Since the Early Pliocene, most of the foredeep experienced the deposition of the thick, sand-dominated turbiditic sequences of the Porto Corsini (Early-Middle Pliocene) and Porto Garibaldi (Middle-Late Pliocene) Formations (Agip, 1982, Ghielmi et al., 2010). The clastic reservoirs of the UGS Fields 1 and 3 are both hosted within sand turbiditic levels of the Porto Garibaldi Formation. The following Upper Pliocene–Pleistocene sand-rich sequences (Asti Group) recorded the transition from deep-marine to continental environments, connected to the latest phases of the Po Plain foredeep infill, up to the deposition of the Holocene clastic deposits in continental environment (alluvium). The overall Late Messinian to the Pleistocene clastic infill of the Po Plain foredeep reached thickness of 7-8 km (Cazzini et al., 2015).

The studied gas fields (Fields 1, 2 and 3) were discovered during the early phases of exploration and research in the Po Plain area, between the 1940s and the 1950s. They were converted to storage activity between the 1960s and the 1980s operating at a maximum injection pressure equal to the reservoirs initial pressure. All three UGS fields are hosted in the culminations of ramp-anticlines that are bounded by steeply dipping, regional thrusts. The seal (caprock) is provided by the Pliocene clay deposits of the Santerno Formation, which extensively cover the structural traps.

3. UGS field description

Field 1 is located in the eastern Po Plain (Fig. 1) at an average depth of 1300 m below sea level (s.s.l.). It was discovered in 1956, and primary production continued with 24 productive wells until 1971; starting from 1975 the field was converted to storage activity. The storage activity is currently managed through more than 50 wells (including storage operative and pressure monitoring wells) with injection and production rates ranging from 3 to 25 MSm^3/d and 5 to 40 MSm^3/d, respectively. The natural gas is hosted within porous sandy levels of the Porto Garibaldi Formation (Middle-Late Pliocene) with an average gross thickness of about 100 m. The seal is guaranteed by the overlying clayey deposits of the Santerno Formation, with an average thickness of 130 m above the trap (see also Benetatos et al. 2020). The simplified subsurface stratigraphy in the field area is shown in Fig. 2. The trap is associated with a strongly asymmetric, elongated anticline with a steep forelimb, bounded to the northeast by a NW-SE striking thrust with northeastward vergence. The trap also has a stratigraphic component: the porous levels pinch-out to the southeast above a structural high formed by the underlying Santerno Formation, defining a narrow non-deposition zone parallel to the fold hinge line. The structural culmination of the trap is found to the northeast of the center of the

field area, close to the bounding fault (Fig. 2a). The extension of the originally mineralized area is approximately 8 km^2.

Field 2 is located in the western Po Plain (Fig. 1) at an average depth of 1400 m s.s.l. It was discovered in 1947, and primary production continued with 23 productive wells until 1967, when the field was converted to storage activity. The storage activity is currently managed through more than 35 wells (including storage operative and pressure monitoring wells) with injection and production rates lower than Field 1. The natural gas is hosted within the reservoir's porous sandy levels of the Caviaga Formation (Early Pliocene), which has an average gross thickness of about 70 m. The seal is guaranteed by the overlying clayey deposits of the Santerno Formation, with a thickness of 400-500 m above the trap. The simplified subsurface stratigraphy in the field area is shown in Fig. 3. The trap is associated with an asymmetric, elongated anticline that is bounded to the south by an E-W striking thrust with southward vergence (Fig. 3a). The structural culmination of the trap is found slightly to the south of the centre of the field area, near the bounding fault. The extension of the originally mineralized area is approximately 6 km^2.

Field 3 is located in the eastern Po Plain (Fig. 1) at an average depth of 1200 m s.s.l. It was discovered in 1959. Primary production started in 1961 and continued with 9 productive wells until 1981, when the field was converted to storage activity in 1985. The storage activity is currently managed through more than 30 wells (including storage operative and pressure monitoring wells) with injection and production rates lower than Field 1 and Field 2. The natural gas is hosted within porous sandy levels of the Porto Garibaldi Fm. (Middle-Late Pliocene) with an average gross thickness of about 25 m; the seal is guaranteed by the overlying clayey deposits of the Santerno Formation, with an average thickness of 75 m above the trap (see also Codegone et al., 2016). The simplified subsurface stratigraphy in the field area is shown in Fig. 4. The trap is associated with an almost symmetric, elongated anticline that is bounded to the northeast by a NW-SE striking thrust with northeastward vergence (Fig. 4a). The structural culmination of the trap is rather flattened and slightly shifted to the northeast of the centre of the field area, near the bounding fault. The extension of the originally mineralized area is approximately 8 km^2.

4. InSAR monitoring: methods and correlation analysis

The InSAR analysis was carried out through the TRE-Altamira SqueeSAR® algorithm (Ferretti et al., 2011), which provides high (millimeter) precision measurements of ground displacement in the form of clouds of measurement points (MP). The SqueeSAR® algorithm analyzes a stack of SAR images acquired over a site and measures the movement of the radar reflectors on the ground surface that

remain visible and coherent throughout the period of the analysis. Radar reflectors can be pointwise targets characterized by highly stable radar return signals (e.g. buildings, rocky outcrops, infrastructures, etc.), or patches of ground presenting a lower but homogenous radar return signal (e.g. rangeland, debris fields, arid areas, etc.). SAR satellites image the ground from ascending and descending orbits, according to the flight direction, respectively from south to north (imaging to the east) and from north to south (imaging to the west).

InSAR measures the projection of the vector of displacement onto the satellite line-of-sight (LOS) and provides 1D measurements along the LOS, which is inclined with respect to the vertical and north-south direction. The 1D (LOS) InSAR results obtained from the ascending and descending orbits over the same area and overlapping periods, are decomposed on a fixed regular grid to obtain the true relative 2D (vertical and east-west planar) components of motion, used in this work. The density and distribution of the identified MPs mainly depend on the resolution of the imagery, the surface characteristics, the surficial changes occurring over time and the topography of the area. The precision of the analysis depends mainly on the correct unwrapping of the phase and estimation/removal of the atmospheric contribution, and increases with the length of the data stack and the coherence of the signal.

In the present study, we analyzed different InSAR datasets acquired from the European Space Agency (ESA) Sentinel-1 twin satellites constellation over a period of 7 years, from Oct 2014 to Oct 2021. The two Sentinel-1 satellites are equipped with a C-band radar sensor (5.6 cm of wavelength), and capture images with a ground pixel of around 5 x 15 m every 12 days (reduced to 6 days by combining both satellites). The datasets analyzed consist of 4 different Sentinel-1 tracks (2 ascending and 2 descending) and around 350 images for each track (Table 1). The seasonal ground movements above the UGS fields are recognized and described using the seasonal amplitude of the ground oscillations, calculated from the displacement time series of the InSAR MPs, which are decomposed into the north-south and east-west components using a regular grid of 50 x 50 m^2

A specific cross-correlation analysis was conducted on the UGS sites of interest to enhance the identification of correlations between the seasonal ground displacements above the fields and the storage activity. During storage operations at the studied UGS sites, the volumes cyclically handled are directly correlated with the cyclical pressure changes within the reservoirs. The correspondence between the recorded minimum and maximum pressures and the handled volumes is consistently verified. The volume parameter represents easily measurable and accessible data, providing a macroscopic and overall view of field management during the storage cycles, and it well correlates with the ground displacement data. Thus, the cross-correlation analysis was based on a comparison between the InSAR-derived displacement time series and the cumulative curve of the

injected/withdrawn gas volumes, aiming to provide a better understanding of the impact of the storage activity on surface deformations.

A mean value of semi-amplitude of seasonality is provided for each identified MP. This value is calculated on the time series of displacement, assuming a seasonal contribution of motion of the following type:

$$A\cos\left(\frac{2\pi}{365}\,T+\varphi\right) \qquad \text{(eq. 1)}$$

where A is the semi-amplitude, T is the time expressed in days, and φ is the seasonality phase referred to the first date of acquisition. Note that the model used to estimate this parameter assumes that the amplitude is constant and corresponds to the average value over the whole monitored period. Thus, it provides an indication of the average amplitude of seasonality. The purpose of the cross-correlation analysis is to correlate the time series of displacement of each MP and the time series of storage volumes. These time series may differ in terms of shape (R) and scale (K). The R index is the cross-correlation factor that quantifies the similarity in the shape of the two curves, without providing information about the magnitude of the motion; it is adjusted for the time delay between the two signals and properly scaled with K. R values range from 0 to 1 , in which 1 represents perfect correlation and 0 no correlation,. The K index (in mm/km^3) is the scaling factor between the InSAR-measured displacements and the amount of gas injection/withdrawal. Negative values of K, means that the InSAR and gas volume curves have opposite signs. High values of R and K indicate a strong correlation between the seasonal displacement and the storage curve. The R and K indexes are calculated with the following equations:

$$\left[\hat{K},\hat{T}\right]=argmin\ \left|\left|S_{sar}\,[t]\ -\ K\cdot W_{gas}[t-T]\right|\right|^2 \qquad \text{(eq. 2)}$$

$$R=\frac{\sum\left(S_{sar}\,[t]\cdot W_{gas}[t-T]\right)}{\sqrt{\sum S_{sar}[t]^2\cdot W_{gas}\,[t-T]^2}} \qquad \text{(eq. 3)}$$

In which $\left|\left|\cdot\right|\right|^2$corresponds to the L2 norm, S_{sar} are the InSAR displacement time-series in mm, W_{gas} is the cumulated injected/withdrawn gas in m^3, t is the time and T the time lag, both in days. The correlation index R indicates how similar the estimated model, $K\cdot W_{gas}[t-T]$, is to the SqueeSAR time-series, and therefore these parameters T and K can be considered meaningful only for high values of R, between 0.5 and 1.

5. Seasonality and Cross-correlation analyses

A strong spatial and temporal correlation is commonly recognized above operative UGS fields between the ground displacements (seasonal uplift/subsidence) and the curve of the storage volumes (e.g., Castelletto et al., 2010; Codegone et al., 2016; Benetatos et al., 2020; Wang et al., 2021; Fibbi et al., 2023). The InSAR analysis of the UGS-related ground deformation is usually based on the assessment of the distribution of the vertical seasonal amplitude values within the monitoring areas, e.g. via 2D amplitude maps and the time series of ground displacements of the MPs.
The InSAR monitoring areas of Field 1, 2 and 3 were divided into concentric sub-areas to analyze the gradients of distribution of the seasonal amplitude, R and K parameters across them with respect of the UGS fields position. Each monitoring area was divided into 5 sub-areas, labeled A, B, C, D, E, with the UGS Field in the center: the boundary of sub-area A corresponds to the UGS field boundary on the ground. The sub-areas outside the reservoir boundary enclose the MPs that are placed between the reservoir area and 500 m (sub-area B), between 500 m and 1 km (sub-area C), between 1 km and 2 km (sub-area D) and over 2 km (sub-area E) from the reservoir boundary.

The maps of seasonal amplitude, R and K, the amplitude histograms and the R-K vs amplitude scatter plots for the vertical component of the ground displacement highlight the specific patterns and trends that characterize each sub-area. In the following, the R and K maps will be provided only for Field 1, as the reference case study, to show the consistency of the areal distribution of the two parameters with respect to the seasonal amplitude trends. For Fields 2 and 3, the distribution of R and K will be only discussed through the scatter plots. The extension of the InSAR monitoring areas is of about 170 km^2 (Field 1 and 3) and about 60 km^2 (Field 2). Note that the distribution of the MPs within each area/sub-area reflects the degree of urbanization (Table 2).

5.1. Results for Field 1

The map of vertical seasonal amplitude (Fig. 5) shows a peak of seasonal displacement within the UGS field boundary. Here, the seasonal oscillations reach maximum amplitude values of ~18 mm, with a radial decreasing trend extending across the A and B sub-areas. It should be noted that the highest values are found slightly NE of the center of sub-area A, decreasing in all directions. The values approach to zero within sub-area A toward the NW and SE. The decreasing trend extends to the sub-area B to the NE, SW and within the non-deposition zone; the highest values are found to the NE (i.e., maximum amplitude ~11 mm), whereas in the other directions the decreasing trend is set on overall lower values with an average amplitude of 1 mm at the southeastern and northwestern edges of the sub-area B.

The histograms in Fig. 5 illustrate the frequency distribution of vertical seasonal amplitude across the different sub-areas. The sub-area A exhibits significantly high seasonal amplitudes, with most data clustered in the >9.5 mm range and a distinct peak in the >12 mm range; lower amplitudes are poorly represented. The sub-area B displays a more even frequency distribution across lower amplitude ranges, with most values <7 mm and no notable peak: the highest frequencies are in the 1-4 mm range. Despite the different number of MPs, the frequency distributions in the sub-areas C, D and E display amplitudes values heavily concentrated in the lowest ranges, with virtually all data showing amplitude <3 mm and an average seasonal amplitude in the order of 1 mm.

The maps of the R and K parameters (Figs. 6-7) show consistent peaks of UGS-related displacement within the UGS field boundary, reaching maximum values of R~1 and K~20 mm/km^3 in correspondence of the seasonal amplitude peak. The R and K parameters decrease radially across the A and B sub-areas, mirroring the seasonal amplitude trend. In the sub-areas C, D and E, where low amplitudes prevail, the R parameter shows a fully random, areal distribution (Fig. 6), and the K parameter exhibits predominantly very low values, as highlighted by the scattered orange-red shades in Fig. 7.

The scatter plots in Fig. 6 show the relationships between the vertical seasonal amplitude and the R parameter across the different sub-areas. Sub-areas A and B exhibit a positive correlation, with seasonal amplitude increasing nonlinearly as R approaches to 1. For low R values, the seasonal amplitude clusters below 1 mm and gradually increases as R increases. For R>0.8, the seasonal amplitude increases more and more steeply. Conversely, the sub-areas C, D and E exhibit a weak positive linear correlation between the parameters within low amplitude ranges. In these areas, nearly all the data have R<0.7. The few outliers suggest some variability but do not substantially alter the overall trends.

The scatter plots in Fig. 7 show the relationships between the vertical seasonal amplitude and the K parameter across the different sub-areas. Sub-areas A and B exhibit a strong, positive linear correlation, with the seasonal amplitude increasing consistently as K moves from 0 to high positive values. A negative linear correlation exists for the few MPs with negative K values and seasonal amplitude mainly <3 mm. Conversely, the sub-areas C, D and E exhibit almost symmetric V-shaped trends, with the data concentrated in the lower ranges of both parameters. In these areas, virtually all of the data have K<5 mm/km^3. Sub-area C has fewer MPs with negative K values compared to D and E, likely due to its sparse dataset. In general, the MPs in these sub-areas follow the linear trends without notable outliers.

A permanent GNSS station was installed at the end of 2008 at the southeastern edge of the field, within sub-area A (location in Fig. 5). The station is equipped with a LEICA GR10 receiver and a TOPCON (TPSCR4 model) antenna with TPSH radome, dual frequency GPS. The historical time series of vertical displacement recorded by the station do not show a clear seasonality (Fig. 8a). After removing the linear trend of vertical displacement, the historical time series was compared with the storage curve (cumulative curve of the injected/withdrawn gas volumes) of Field 1 (Fig. 8b). The GNSS data do not exhibit any appreciable correlation with storage activity. Instead, the vertical movements can be primarily attributed to variations in the hydrological load (see Benetatos et al., 2020 for further details). The InSAR data near the station report average seasonal amplitude of 2.6 mm, R=0.7 and K=3 mm/km^3. These results are consistent with the station's position near the edge of the InSAR seasonal amplitude variation, and provide further constraints to the observed decreasing trend in the vertical seasonal displacement within the sub-area A.

5.2. Results for Field 2

The map of the vertical seasonal amplitude (Fig. 9) shows the highest values (~9 mm) within the UGS field boundary, with a radial decreasing trend across the A, B and C sub-areas. The peak of seasonal displacement is measured slightly to the south of the center of sub-area A and decreases in all directions, reaching near-zero values to the west. It should be noted that the easternmost part of the sub-area A has no MPs because it is a vegetated area including a large fluvial region. Low amplitude values were here expected, according with the observed decreasing trend; supporting this, low amplitude values (approaching to zero) are observed in the surroundings and further east in the sub-area B. The decreasing trend extends into the sub-area B to the north and S-SE: the highest amplitude values are observed south of the field (amplitude ~6 mm). In the northern and southeastern part of the sub-area B, the decreasing trend is set on overall lower value ranges, with most data showing amplitude <3.5 mm. The sub-area C exhibits a slight decreasing trend toward the north and SE, but in lower ranges than the A and B sub-areas, with most data showing amplitude <3 mm. The MPs in the sub-areas D and E predominantly exhibit amplitudes ≤2 mm.

The amplitude histogram of the sub-area A (Fig. 9) shows overall higher values than the other sub-areas, , but, unlike Field 1, it lacks a distinct frequency peak in the higher amplitude ranges. The sub-area B displays an even frequency distribution across lower amplitude ranges than sub-area A, with most of the data in the <5 mm range and a rough multimodal distribution. Despite differences in the number of MPs, the sub-areas C, D and E show similar frequency distributions that markedly differ from to those of sub-areas A and B. The C sub-area shows a slightly higher frequency peak in the 1-1.5 mm range, but in all three sub-areas, the amplitudes are consistently concentrated in the lowermost ranges, with nearly all the data showing amplitudes <2-3 mm, and an average seasonal amplitude in the order of 1 mm.

The scatter plots of seasonal amplitude vs R parameter (Fig. 10) show a positive correlation between in the sub-areas A and B, with an increasing nonlinearity as R approaches to 1. For low R values, the seasonal amplitude clusters below 1 mm and gradually increases as R increases. For R>0.8, the seasonal amplitude increases more steeply. Conversely, the sub-areas C, D and E show weak, positive linear correlation between the parameters within low amplitude ranges. Most data from the sub-area C have R<0.8, while more than almost all of the data of the sub-areas D and E have R<0.6. The few outliers suggest some variability but do not substantially alter the overall trends.

The scatter plots of seasonal amplitude vs K parameter (Fig. 11) exhibit a strong, positive linear correlation in the sub-areas A and B, with the majority of the data in the positive range of K. In the sub-area B, a few MPs exhibit a negative linear correlation for negative K values, with seasonal amplitude mainly <1 mm. Conversely, the scatter plots of the sub-areas C, D and E show a symmetric V-shaped trend, with the data concentrated in the lower ranges of both the parameters. In these areas, almost all of data have K<5 mm/km^3. In general, the MPs follow the linear trends with few outliers.

5.3. Results for Field 3

The map of the vertical seasonal amplitude (Fig. 12) shows the highest values (~7 mm) within the UGS field area, with a radial decreasing trend across the A and B sub-areas. The peak of seasonal displacement is measured in the center of the sub-area A, and decreases in all directions, reaching near-zero values toward NW and SE. The decreasing trend extends into the sub-area B to the NE and SW, where it is set on overall lower values, with most data showing amplitude <4 mm. The MPs in the sub-areas C, D and E predominantly exhibit amplitudes ≤2 mm.

The amplitude histograms of the sub-area A exhibit overall higher values than the other sub-areas (Fig. 12). Like Field 2, Field 3 does not exhibit a frequency peak in the higher amplitude range, but rather it displays a bimodal data distribution with two peaks at ~1 mm and ~5 mm. Despite differences in the number of MPs, the histograms of the sub-areas B, C, D and E show similar frequency distributions, that markedly differ from to those of sub-area A: the amplitudes are consistently concentrated in the lowermost value ranges, with the vast majority of the data in the <3 mm range and an average seasonal amplitude in the order of 1 mm.

The scatter plots of seasonal amplitude vs R parameter (Fig. 13) exhibit a positive correlation in the sub-area A with a certain nonlinearity as R approaches to 1. For low R values, the seasonal amplitude clusters below 1 mm and increases faster as R gradually increases. The sub-areas B, C, D and E show a weak, positive linear correlation within low amplitude ranges. Nearly all the data

concentrate in the R<0.7 range. The few outliers suggest some variability but do not substantially alter the overall trends.

The scatter plots of seasonal amplitude vs K parameter (Fig. 14) exhibit clear V-shaped trends. The scatter plot of the A sub-area shows a prevailing positive linear correlation, with most of the data in the positive range of K, and the seasonal amplitude increasing consistently as K moves from 0 to high positive values; a negative linear correlation exists for the few MPs with negative values of K and seasonal amplitude mainly <3 mm. The sub-areas B, C, D and E exhibit a notable concentration of data in the lower ranges of both the parameters, with almost all data in the K<10 mm/km^3 range. In general, the MPs follow the linear trends with no outliers.

6. Thresholds definition

The described data allowed to characterize the InSAR signal in the UGS-monitored areas in terms of vertical seasonal amplitude and cross-correlation parameters (R and K). In particular, the presented method allows for the discrimination between the part of the signal that effectively records the UGS activities and the background noise. The described MPs maps show that the sub-areas D and E (>1 km from the UGS field boundaries) consistently exhibit random distributions of vertical seasonal amplitude, R and K in their lowest ranges, with no directional trends linked to the sub-area A, where the peak of UGS-related displacements is located. These observations suggest the absence of correlation with UGS activities. The histograms and scatter plots confirm that the frequency distributions of vertical seasonal amplitude, R and K in the subareas D and E are not affected by UGS-related displacements, unlike the sub-area A. The "undisturbed" character of the R and K frequency distributions in the subareas D and E serves as a reference to characterize the background-noise signal in the UGS monitoring areas.

As outlined above, the frequency distributions show that almost all the MPs in the sub-areas D and E have R<0.7 and K<5 mm/km^3 (Field 1), R<0.6 and K<5 mm/km^3 (Field 2), R<0.7 and K<10 mm/km^3 (Field 3) (see Table 3). These values are considered the threshold values for R and K parameters that identify the site-specific, upper limits of the background noise. The MPs with R and K values above these thresholds record UGS-related displacements that superimpose and exceed the background noise, indicating an effective correlation between the ground movements and the storage activities.

The frequency distributions for the sub-area C of the Field 1 and 3 are similar to those of the sub-areas D and E. Only the Field 2 shows clues of a possible extension of the UGS-related displacement trend into the sub-area C, but within a very low amplitude range, similar to the sub-areas D and E.

The maps in Figs. 15, 16 and 17 show the spatial distributions of the MPs with R and K values above the thresholds (indicated in black): they identify the effective influence area of the storage activity on the ground surface for each UGS field. Most MPs recording the UGS-related displacements for Field 1 (Fig. 15a-b) and Field 2 (Fig. 16a-b), and almost all MPs recording the UGS-related displacements for Field 3 (Fig. 17a-b), are located within the field areas. The time series of vertical displacement for the MPs at the peaks of vertical seasonal amplitude exhibit a marked sinusoidal trend of movement with a strong correlation with storage activities (e.g. Fig. 15c, Fig. 16c and Fig. 17c).

The UGS-related vertical displacements do not reach the field boundaries along the major axes of the traps (NW-SE for Field 1 and Field 3; E-W for Field 2), except for the southeastern edge of Field 1, corresponding to the narrow non-deposition zone of the trap, where a few MPs record UGS-related displacements. No MPs are available in the easternmost part of the Field 2 area, but R and K values below the thresholds are expected, based on the decreasing amplitude trend (reaching very low values further east) and the comparison with the Field 1 and Field 3. Along the minor axes of the traps, the UGS influence area extends outside the field boundaries, up to ~500 m for Field 1 (NE-SW direction), ~500 m (K map) and ~1 km (R map) for Field 2 (N-S direction), and ~400 m for Field 3 (NE-SW direction).

The influence area identified by the R map is slightly larger than that of the K map for Field 1 and Field 2, especially toward the SW and SE (Field 1) and toward the north and SE (Field 2). The time series of vertical displacement for the MPs located within the UGS influence area of the R maps, but outside the influence area of the K maps (Fig. 15d and Fig. 16d), show irregular, low-amplitude seasonal signal. For Field 1, the Fig. 15d refers to MPs close to the GNSS station (location in Fig. 15b), which does not highlight vertical seasonal oscillations correlated with storage activities: such results are consistent with the K map. For Field 3, the R and K maps provide consistent extensions of the UGS influence area. The time series of vertical displacement for the MPs located at the edge of the UGS influence areas show UGS-related oscillations but in a lower amplitude range (Fig. 17d). The time series of vertical displacement outside the influence area (~900 m from Field 1 and Field 2, and ~600 m from Field 3) confirm the absence of any seasonal trend (Figs. 15e, 16e, 17e).

7. Discussion

The described analysis was based on InSAR data acquired over three operative UGS fields corresponding to elongated anticline traps bounded by frontal thrusts. The anticlines exhibit different degrees of structural asymmetry: the anticline of Field 1 is highly asymmetric, with a steep forelimb

and the structural culmination very close to the bounding thrust; the anticline of Field 3 is nearly symmetric, with a flattened structural culmination slightly shifted toward the bounding thrust; the anticline of Field 2 exhibits intermediate features. These fields also share comparable reservoir extension, depth, lithology, and overburden stratigraphy.

The distribution of the vertical UGS-related displacements shows similar trends across the three monitored areas: the peak of vertical seasonal displacement is located within the field areas and decreases radially. The geometric similarity between the traps and the deformation trends allowed us to apply the same analytic approach. The cross-correlation analysis confirmed that the highest values of the cross-correlation parameters R and K are consistently concentrated within the field boundaries (subareas A), decreasing radially in all directions. The peak of vertical seasonal oscillation is characterized by R=0.98, K=19.6 mm/km^3 (Field 1), R=0.96, K=19.3 mm/km^3 (Field 2), and R=0.97, K=27.2 mm/km^3 (Field 3).

The outermost parts of the monitored areas, more than 1 km from the field boundaries (sub-areas D and E), consistently exhibit: (i) the absence of directional trends, (ii) the prevalence of low amplitudes (≤2-3 mm) with an average value in the order of 1 mm, (iii) a fully random distributions of R values across a wide range, and (iv) a prevalence of low K values. These characteristics confirm that the MPs more than 1 km away from the field areas are unaffected by UGS activities and record the "undisturbed signal" of the monitored areas. Their frequency distributions were used to define threshold values on R and K, representing the upper limits of the background noise. The results indicate that the estimated threshold values are site-specific: R=0.7 and K=5 mm/km^3 (Field 1), R=0.6 and K=5 mm/km^3 (Field 2), R=0.7 and K=10 mm/km^3 (Field 3). The MPs with R and K values exceeding these thresholds provide evidence of UGS-related displacements: the spatial distribution of such MPs identifies the effective influence area of the UGS activity.

For all three fields, the influence area is mostly contained within the field areas, with a minor extension outside in the direction perpendicular to the bounding fault of the geological trap. Conversely, in the direction parallel to the fault (trap major axis), UGS-related displacement values diminish before reaching the reservoir boundary. Possible explanations for this behaviour could include the characteristics of the surrounding aquifer. The threshold values of Field 1 identify an influence area which extends outside the field boundary up to a maximum distance of ~500 m. The influence area identified by the R threshold is slightly larger. The GNSS data corroborate the K threshold results, attesting that R slightly overestimates the extension of the influence area. The threshold values of Field 2 identify an influence area which extends outside the field boundary up to a maximum distance of ~500 m (K threshold) and ~1 km (R threshold). Also in this case, the influence area identified by the R threshold is slightly more extensive, particularly towards the north and SE. The observations from Field 1 suggest that K provide more reliable estimations. The threshold values

of Field 3 identify an influence area which extends quite symmetrically outside the field boundary up to a maximum distance of ~400 m. In this case, the R and K maps provide consistent extensions of the UGS influence area. The time series of vertical displacement confirm that the MPs with R and K values below the thresholds lack any evidence of UGS-related displacement.

Finally, the peak of the ground oscillation for Field 1 and Field 2 is offset from the centre of the field areas. Fig. 18 shows the MPs with R≥0.9 compared with the structural map of the buried traps. Almost all the MPs are concentrated within the field areas. The peak of oscillation for Field 1 and Field 2 is shifted towards the bounding fault of the trap. This asymmetry reflects the structural asymmetry of the traps, which determines the position of the crest where most of the storage wells intersect the reservoir. As a result, the higher UGS-related amplitudes measured outside the field areas are concentrated near the bounding faults, where oscillation peaks abruptly stop due to the faults presence. Conversely, Field 3, with its symmetric trap, exhibits the peak of oscillation almost in the centre of the field area. These findings could provide insights into the role of the trap geometry and of the bounding faults in confining the expected major UGS-related uplift and subsidence phenomena at the surface.

8. Conclusions

The present study proposes an analytical methodology to identify the influence area of the UGS-related ground deformations above three operative UGS fields in the Po Plain (Italy). The methodology is based on the characterization of the InSAR monitoring data in terms of vertical seasonal amplitude (measuring the amount of average seasonal displacement) and R-K cross-correlation parameters (quantifying the correlation between the seasonal displacement and the UGS activity), focusing on the vertical component of the ground deformations. The InSAR dataset comprises images acquired by the Sentinel-1 satellites over the 2015-2021 period.

The studied UGS fields were selected based on their similar geological complexities to ensure that the distribution of ground deformations relative to the geological features was geometrically comparable, enabling the application of a consistent analytical approach. The case studies correspond to elongated, anticline traps bounded by frontal thrusts (i.e., buried ramp anticlines), and also share similar reservoir extension (6-8 km^2), depth (1200 to 1400 m s.s.l.), lithology (coarse-grained and sand-rich turbidites), and overburden stratigraphy (including, in particular, the clayey caprock). The described analyses confirm that the MPs in the outermost part of the monitored areas (>1 km from the fields) are not affected by UGS-related ground displacements and record the “undisturbed signal”: these MPs were used as reference to identify threshold values for R and K that

606 are site-specific. The MPs with R and K values exceeding these thresholds identify the effective
607 influence area of the storage activity.
608
609 Our findings show that, with the UGS injection/ withdrawal plan implemented until 2021, the influence
610 areas of the studied UGS cases are mostly confined within the field areas and only a minor part
611 extends outside. Along the major axis of the traps/fields, the measurable UGS-related displacements
612 cease before reaching the field boundaries, whereas transversally these extend outside up to a few
613 hundred meters (~400-500 m). The R and K thresholds for Field 3 provide consistent extensions of
614 the influence area, while the R thresholds for Field 1 and Field 2 identify slightly more extensive
615 influence areas than the K thresholds. The data from the GNSS station at the edge of Field 1 are
616 consistent with the K threshold results. It attests that R tends to slightly overestimate the extension
617 of the influence area, that can be considered a conservative result. Furthermore, the data indicate
618 that the position of the displacement peaks reflects the structural asymmetry of the traps.
619 The proposed analytical methodology allows for rapid and precise identification of the areas
620 experiencing uplift/subsidence at surface due to the underground operations at the reservoir depth
621 by analyzing R-K parameters derived from the InSAR data. The accurate definition of the influence
622 area applied to geomechanical simulations can significantly improve the calibration of the
623 geomechanical parameters, and. Additionally, it can serve as a monitoring tool by comparing the
624 results of geomechanical simulations with the observed outcomes. Significant discrepancies
625 between observed and predicted deformation areas might indicate groundwater movement in
626 shallower stratigraphic layers, hydraulically separated from the reservoir.
627
628 The methodology could be expanded also to reservoir types dedicated to underground fluid storage
629 characterized by other geological features and ground deformation trends, providing valuable
630 insights and observations. For example, a different nature or geometry of the trap (e.g. stratigraphic
631 traps) should require drawing different geometries of the analysis sub-areas. A comprehensive
632 understanding of the structural and stratigraphic complexities of the reservoir and surrounding
633 formations, along with the deformation trends, remains essential to adapt - and properly apply - the
634 proposed method. The use of different satellites working with other radar wavelengths could provide
635 new insights on the influence area definition. Moreover, deploying more satellites with diverse
636 viewing angles could also enhance the available information from both temporal and spatial
637 resolution points of view.
638
639
640 **Acknowledgements**
641

642 The authors wish to thank Snam S.p.A. - Stogit Division for providing the data used in this study and
643 for permitting the publication of this manuscript, and Professors Piras M. and Dabove P. of the
644 Politecnico di Torino (Department of Environmental, Land and Infrastructure Engineering) for their
645 work on the GNSS data analysis. They would also like to express their gratitude to the two
646 anonymous reviewers for their careful assessment; their comments and suggestions greatly
647 contributed to improving the manuscript.
648
649
650 **References**
651
652 Agip S.p.A., 1982. Lessico delle Formazioni del bacino padano orientale. In: Cremonini G, Ricci
653 Lucchi F (eds) Guida alla Geologia del margine appenninico-padano. Guide geologiche
654 regionali. Soc. Geol. Ital., Rome, 205–247.
655 Amadori, C., Garcia-Castellanos, D., Toscani, G., Di Giulio, A., Fantoni, R., and Ghielmi, M., 2017.
656 Restoration of paleo-shorelines through lithospheric 3D modeling and backstripping analysis:
657 The example of the Po Plain-Northern Adriatic region during Late Messinian sea-level drop.
658 Offshore Mediterranean Conference and Exhibition (OMC) 2017, 29–31 March 2017, Ravenna
659 (Italy).
660 Amadori, C., Garcia-Castellanos, D., Toscani, G., Sternai, P., Fantoni, R., Ghielmi, M., and Di Giulio,
661 A., 2018. Restored topography of the Po Plain-Northern Adriatic region during the Messinian
662 base-level drop—Implications for the physiography and compartmentalization of the palaeo-
663 Mediterranean basin. Basin Res., 30, 1247–1263. https ://doi.org/10.1111/bre.12302
664 Amadori, C., Toscani, G., Di Giulio, A., Maesano, F.E., D'Ambrogio, C., Ghielmi, M., Fantoni, R.,
665 2019. From cylindrical to non-cylindrical foreland basin:Pliocene–Pleistocene evolution of the
666 Po Plain–Northern Adriatic basin (Italy). Basin Res., 31(5), 991-1015.
667 https://doi.org/10.1111/bre.12369
668 Antoncecchi, I., Ciccone, F., Rossi, G., Agate, G., Colucci, F., Moia, F., Manzo, M., Lanari, R.,
669 Bonano, M., De Luca, C., Calabrese, L., Perini, L., Severi, P., Pezzo, G., Macini, P., Benetatos,
670 C., Rocca, V., Carminati, E., Billi, A., Petracchini, L., 2021. Soil deformation analysis through
671 fluid-dynamic modelling and DInSAR measurements: a focus on groundwater withdrawal in the
672 Ravenna area (Italy). Boll. Geof. Teor. Appl., 62, 301-316. https://doi.org/10.4430/bgta0350
673 ARPAE (Agenzia Prevenzione Ambientale Energia Emilia-Romagna), 2018. Rilievo Della
674 Subsidenza Nella Pianura Emiliano-Romagnola Seconda Fase, Relazione Finale. Bologna;
675 ARPAE: Bologna, Italy, 2018; pp. 105.
676 Balestro, G., Festa, A., De Caroli, S., Barbero, E., Borghi, A., Gianotti, F., 2022. Multistage
677 tectono-stratigraphic evolution of the Canavese Intracontinental Suture Zone: New constraints

on the tectonics of the Inner Western Alps. Geosci. Front., 13, 101448. https://doi.org/10.1016/j.gsf.2022.101448

Benetatos, C., Codegone, G., Deangeli, C., Giani, G., Gotta, A., Marzano, F., Rocca, V., Verga, F., 2017. Guidelines for the study of subsidence triggered by hydrocarbon production, Geoing. Amb. Miner., 152(3), 85-96, ISSN: 11219041.

Benetatos, C., Codegone, G., Ferraro, C., Mantegazzi, A., Rocca, V., Tango, G., Trillo, F., 2020. Multidisciplinary Analysis of Ground Movements: an Underground Gas Storage case study. Rem. Sens., 12, 3487; doi:10.3390/rs12213487

Bertoni, W., Brighetti, G., Gambolati, G., Ricceri, G., Vuillermin, F., 1995. Land subsidence due to gas production in the on- and off-shore natural gas fields of the Ravenna area, Italy. IAHS Publ., 234, 13-20.

Bitelli, G., Bonsignore, F., Del Conte, S., Franci, F., Lambertini, A., Novali, F., Severi, P., Vittuari, L., 2020. Updating the subsidence map of Emilia-Romagna region (Italy) by integration of SAR interferometry and GNSS time series: The 2011–2016 period. Proc. IAHS 2020, 382, 39–44.

Boccaletti, M., Corti, G., Martelli, L., 2011. Recent and active tectonics of the external zone of the Northern Apennines (Italy). Int. J. Earth Sci. (Geol Rundsch). http:// dx.doi.org/10.1007/s00531-010-0545-y

Braun, T., Danesi, S., Morelli, A., 2020. Application of monitoring guidelines to induced seismicity in Italy. J. Seismol., 24, 1015–1028. https://doi.org/10.1007/s10950-019-09901-7

Calabrese, L., Luciani, P., Perini, L., 2021. A review of impact of subsidence induced by gas exploitation on costal erosion in Emilia-Romagna, Italy. Boll. Geof. Teor. Appl., 62, 279-300. doi: 10.4430/bgta0356.

Carminati, E., Martinelli, G., 2002. Subsidence rates in the Po Plain (northern Italy): the relative impact of natural and anthropic causation. Eng. Geol., 66, 241-255.

Carminati, E., Doglioni, C., Scrocca, D., 2003. Apennines subduction-related subsidence of Venice. Geophys. Res. Lett., 30(13), 1717. doi:10.1029/2003GL017001

Castelletto, N., Ferronato, M., Gambolati, G., Janna, C., Teatini, P., Marzorati, D., Cairo, E., Colombo, D., Ferretti, A., Bagliani, A., Mantica, S., 2010. 3D geomechanics in UGS projects. A comprehensive study in northern Italy. 44th US Rock Mechanics Symposium and 5th U.S.-Canada Rock Mechanics Symposium, held in Salt Lake City, UT June 27–30, 2010.

Cazzini, F., Dal Zotto, O., Fantoni, R., Ghielmi, M., Ronchi, P. and Scotti, P., 2015. Oil and gas in the Adriatic foreland, Italy. J. Pet. Geol., 38, 255–279.

Cenni, N., Viti, M., Baldi, P., Mantovani, E., Bacchetti, M., Vannucchi, A., 2013. Present vertical movements in central and northern Italy from GPS data: possible role of natural and anthropogenic causes. J. Geodyn., 71, 74-85.

Codegone, G., Rocca, V., Verga, F., Coti, C., 2016. Subsidence Modelling Validation Through Back Analysis for an Italian Gas Storage Field. Geot. Geol. Eng., 34, 1749-1763. https://doi.org/10.1007/s10706-016-9986-9

Dacome, M.C., Miandro, R., Vettorel, M., Roncari, G., 2015. Subsidence monitoring network: An Italian example aimed at a sustainable hydrocarbon EandP activity. In: Proceedings of the International Association of Hydrological Sciences (IAHS), Nagoya, Japan, 15–19 November 2015; Copernicus GmbH: Göttingen, Germany (2015), 372, 379–384.

Dercourt, J., Zonenshain, L.P., Ricou, L.E., Kazmin, V.G., Le Pichon, X., Knipper, A.L.,Grandjacquet, C., Sbortshikov, I.M., Geyssant, J., Lepvrirer, C., Pechersky, D.H., Boulin, J., Sibuet, J.C., Savostin, L.A., Sorokhtin, O.,Westphal, M., Bazchenov, M.L., Lauer, J.P., Biju-Duval, B., 1986. Geological evolution of the Tethys belt from Atlantic to the Pamirs since the Lias. In: Aubouin, J., Le Pichon, X., Monin, A.S. (Eds.), Evolution of the Tethys. Tectonophysics, 123, 241-315.

Dialuce, G., Chiarabba, C., Di Bucci, D., Doglioni, C., Gasparini, P., Lanari, R., Priolo, E., Zollo, A., 2014. Indirizzi e linee guida per il monitoraggio della sismicità, delle deformazioni del suolo e delle pressioni di poro nell'ambito delle attività antropiche. GdL MISE, Roma. unmig.mise.gov.it/unmig/agenda/upload/85_238.pdf (English version at: https://unmig.mise.gov.it/images/docs/151_238.pdf; last accessed: August 20, 2019).

Doglioni, C., 1993. Some remarks on the origin of foredeeps, Tectonophysics, 228, 1–22.

Pieri, M., Groppi, G., 1981. Subsurface Geological Structure of the Po Plain, Italy. In Progetto Finalizzato Geodinamica; Consiglio Nazionale Delle Ricerche: Rome, Italy (1981), 414, 1–13.

Fantoni, R., Franciosi, R., 2009. Estensione mesozoica e compressione cenozoica nell'avampaese padano–adriatico. Abstract e Poster Natura e geodinamica della litosfera nell'alto Adriatico Venezia, Palazzo Loredan 5–6 Novembre 2009. Rend. online Soc. Geol. It., 9, 28–31.

Fantoni, R., Franciosi, R., 2010. Tectono-sedimentary setting of the Po Plain and Adriatic foreland. Rend. Linc., 21, 197–209.

Fantoni, R., Bersezio, R., Forcella F., 2004. Alpine structure and deformation chronology at the Southern Alps-Po Plain border in Lombardy. It. J. Geosc., 123(3), 463–476.

Ferretti, A., Fumagalli, A., Novali, F., Prati, C., Rocca, F., Rucci, A. 2011. A New Algorithm for Processing Interferometric Data-Stacks: SqueeSAR. IEEE T. Geoscience and Remote Sensing. 49. 3460-3470. 10.1109/TGRS.2011.2124465.

Ferronato M., Castelletto, N., Gambolati, G., Janna, C., Teatini, P., 2013. II cycle compressibility from satellite measurements. Geotechnique, 63(6), 479–486. http://dx.doi.org/10.1680/geot.11.P.149

Festa A., Dilek., Y., Codegone G., Cavagna, S., Pini, G.A., 2013. Structural Anatomy of the Ligurian Accretionary Wedge (Monferrato, NW-Italy), and Evolution of Superposed Mélanges. Geol. Soc. Am. Bull., 125 (9/10), 1580-1598. Doi: 10.1130/B30847.1

Festa A., Fioraso G, Bissacca E., Petrizzo M.R., 2015. Geology of the Villalvernia- Varzi Line between Scrivia and Curone valleys (NW Italy). J. Maps, 11 (1), 39-55. Doi: 10.1080/17445647.2014.959569.

Fjær, E., Holt, R.; Horsrud, P., Raaen, A., Risnes, R., 2008. Chapter 3 Geological aspects of petroleum related rock mechanics. In: Developments in Petroleum Science, 2nd ed.; Elsevier BV: Amsterdam, The Netherlands (2008), 53, 103–133.

Fibbi, G., Beni, T., Fanti, R., Del Soldato, M., 2023. Underground Gas Storage Monitoring Using Free and Open Source InSAR Data: A Case Study from Yela (Spain). Energies, 16, 6392. https://doi.org/10.3390/en16176392

Gambolati, G., Teatini, P., 2015. Geomechanics of subsurface water withdrawal and injection. Water Resour. Res., 51, 3922-3955, doi: 10.1002/2014WR016841.

Ghielmi, M., Minervini, M., Nini, C., Rogledi, S., Rossi, M., Vignolo, A., 2010. Sedimentary and tectonic evolution in the eastern Po-Plain and northern Adriatic Sea area from Messinian to Middle Pleistocene (Italy). Rend. Fis. Acc. Linc., 21(Suppl 1), S131–S166. doi:10.1007/s12210-010-0101-5

Ghielmi, M., Minervini, M., Nini, C., Rogledi, S., Rossi, M., 2013. Late Miocene–Middle Pleistocene sequences in the Po Plain–Northern Adriatic Sea (Italy): the stratigraphic record of modification phases affecting a complex foreland basin. Mar. Pet. Geol., 42, 50–81. doi:10.1016/j.marpetgeo.2012.11.007

Giani, G.P., Gotta, A., Marzano, F., Rocca, V., 2017. How to Address Subsidence Evaluation for a Fractured Carbonate Gas Reservoir Through a Multi-disciplinary Approach. Geot. Geol. Eng., 35, 2977-2989, ISSN: 0960-3182, doi: 10.1007/s10706-017-0296-7

Irace, A., Marcelli, I., Fioraso, G., Festa, A., Catanzariti, R., Raco, B., Menichini, M., Masetti, G., Brussolo, G., Doveri, M., 2024. Subsurface geology of the Torino metropolitan area (Westernmost Po Plain, NW Italy). J. Maps, 20 (1), 2391963. Doi: 10.1080/17445647.2024.2391963.

Livani, M., Petracchini, L., Benetatos, C., Marzano, F., Billi, A., Carminati, E., Doglioni, C., Petricca, P., Maffucci, R., Codegone, G., Rocca, V., Verga, F., Antoncecchi, I., 2023. Subsurface geological and geophysical data from the Po Plain and the northern Adriatic Sea (north Italy), Earth Syst. Sci. Data, 15, 4261–4293, https://doi.org/10.5194/essd-15-4261-2023.

Palano, M., Pezzo, G., Serpelloni, E.,, Devoti, R., D'Agostino, N., Gandolfi, S., Sparacino, F., Anderlini, L., Poluzzi, L., Tavasci, L., Macini, P., Pietrantonio, G., Riguzzi, F., Antoncecchi, I., Ciccone, F., Rossi, G., Avallone, A., Selvaggi, G., 2020. Geopositioning time series from offshore platforms in the Adriatic Sea. Scient. Data, 7, 373. https://doi.org/10.1038/s41597-020-00705-w

Picotti, V., Prosser, G., Castellarin, A., 1995. Structures and kinematics of the Giudicarie – Val Trompia fold and thrust belt (Central Southern Alps, Northern Italy). Mem. Soc. Geol., 47, 95-109.

Pieri, M., Groppi, G., 1981. Subsurface geological structure of the Po Plain, Italy. CNR Prog. Fin. Geodin. 414, 1–13.

Scardia, G., Festa, A., Monegato, G., Pini, R., Rogledi, S., Tremolada, F., Galadini, F., 2015. Evidence for late Alpine tectonics in the Lake Garda area (northern Italy) and seismogenic implications. GSA Bull., 27(1-2), 113-130. https://doi.org/10.1130/B30990.1

Severi, P., Mazzoni, R., Martelli, L., 2020. Oil and gas activities in Emilia-Romagna Region (Italy): land deformation and territory protection. Boll. Geof. Teor. Appl., 62(2), 269-278; June 2021. doi: 10.4430/bgta0327

Severi, P., 2021. Soil uplift in the Emilia-Romagna plain (Italy) by satellite radar interferometry. Bull. Geoph. Ocean., 62(3), 527-542.

Settari, A., Walters, D.A., Stright, D.H., Aziz, K., 2008. Numerical techniques used for predicting subsidence due to gas extraction in the North Adriatic Sea. Pet. Sci. Technol., 26, 1205–1223

Teatini, P., Ferronato, M., Gambolati, G., Gonella, M., 2006. Groundwater pumping and land subsidence in the Emilia-Romagna coastland, Italy: Modelling the past occurrence and the future trend. Water Resour. Res., 42. https://doi.org/10.1029/2005WR004242.

Teatini, P., Castelletto, N., Ferronato, M., Gambolati, G., Janna, C., Cairo, E., Marzorati, D., Colombo, D., Ferretti, A., Bagliani, A., Bottazzi, F., 2011. Geomechanical response to seasonal gas storage in depleted reservoirs: A case study in the Po River basin, Italy. J. Geoph. Res., 116. https://doi.org/10.1029/2010JF001793

Toscani, G., Bonini, L., Ahmad, M.I., Bucci, D.D., Giulio, A.D., Seno, S., Galuppo, C., 2014. Opposite verging chains sharing the same foreland: kinematics and interactions through analogue models (Central Po Plain, Italy). Tectonophysics, 633(1), 268-282.

Turrini, C., Toscani, G., Lacombe, O., Roure, F., 2016. Influence of structural inheritance on foreland-foredeep system evolution: An example from the Po valley region (northern Italy). Mar. Pet. Geol., 77, 376–398. https ://doi.org/10.1016/j.marpetgeo.2016.06.022

Wang, Y., Feng, G., Li, Z., Xu, W., Zhu, J., He, L., Xiong, Z., Qiao, X., 2022. Retrieving the displacements of the Hutubi (China) underground gas storage during 2003–2020 from multi-track InSAR. Rem. Sens. Env., 268, 112768

Figure and Table captions

Figure 1. (a) Simplified structural map of the Po Plain. The black lines represent the buried thrusts of the Northern Apennines; the yellow lines represent the buried thrust pf of the Southern Alps; the red dashed line indicates the trace of the geological cross section in (b); the red squares indicate the location of the studied UGS fields. SA: South Alpine fronts; MF: Monferrato fronts; EF: Emilia fronts; FF: Ferrara fronts (modified after Livani et al., 2023). (b) Simplified geological section across the Po Plain; the black dots indicate the approximate structural position of the studied anticline traps (UGS Field 1, 2, 3) with respect to the buried thrust fronts of the Northern Apennines and Southern Alps (modified after Livani et al., 2023).

Figure 2. Field 1. (a) Simplified map of the structural top; (b) cross section derived from the 3D seismic volume crossing the trap (see Benetatos et al., 2020); (c) simplified subsurface stratigraphy in the field area (green color: UGS reservoir).

Figure 3. Field 2. (a) Simplified map of the structural top; (b) simplified subsurface stratigraphy in the field area (green color: UGS reservoir).

Figure 4. Field 3. (a) Simplified map of the structural top; (b) simplified subsurface stratigraphy in the field area (green color: UGS reservoir).

Figure 5. (a) Map of the vertical seasonal amplitude: the solid line represents the boundary of Field 1 (sub-area A), the dashed lines represent the outer boundaries of the sub-areas B, C, D (the names of the sub-areas are indicated in the black squares). The red circle indicates the location of the GNSS station. (b) Statistics (minimum, maximum, average values and standard deviation) and histograms of the seasonal amplitude distribution in the sub-areas A, B, C, D, E.

Figure 6. (a) Map of the R parameter: the solid line represents the boundary of Field 1 (sub-area A), the dashed lines represent the outer boundaries of the sub-areas B, C, D; (b) Scatter plots of R vs seasonal amplitude in the sub-areas A, B, C, D, E. The names of the sub-areas are indicated in the black squares.

Figure 7. (a) Map of the K parameter: the solid line represents the boundary of Field 1 (sub-area A), the dashed lines represent the outer boundaries of the sub-areas B, C, D; (b) Scatter plots of K vs seasonal amplitude in the sub-areas A, B, C, D, E. The names of the sub-areas are indicated in the black squares.

Figure 8. Historical time series of vertical displacement measured by the GNSS station. (a) Difference between the estimated and reference coordinates. (b) Comparison between the de-trended historical time series and the storage curve (red line).

Figure 9. (a) Map of the vertical seasonal amplitude: the solid line represents the boundary of Field 2 (sub-area A), the dashed lines represent the outer boundaries of the sub-areas B, C, D. (b) Statistics (minimum amplitude, maximum amplitude, average amplitude and standard deviation) and histograms of the seasonal amplitude distribution in the sub-areas A, B, C, D, E.

Figure 10. Scatter plots of R vs seasonal amplitude for Field 2. A, B, C, D, E: sub-areas of analysis (location in Fig. 9).

Figure 11. Scatter plots of K vs seasonal amplitude for Field 2. A, B, C, D, E: sub-areas of analysis (location in Fig. 9).

Figure 12. (a) Map of the vertical seasonal amplitude: the solid line represents the boundary of the Field 3 (sub-area A), the dashed lines represent the outer boundaries of the sub-areas B, C, D. (b) Statistics (minimum, maximum, average values and standard deviation) and histograms of the seasonal amplitude distribution in the sub-areas A, B, C, D, E.

Figure 13. Scatter plots of R vs seasonal amplitude for Field 3. A, B, C, D, E: sub-areas of analysis (location in Fig. 12).

Figure 14. Scatter plots of K vs seasonal amplitude for Field 3. A, B, C, D, E: sub-areas of analysis (location in Fig. 12).

Figure 15. Maps of the R (a) and K (b) parameters in the Field 1 monitoring area; the solid line represents the boundary of the field. (c), (d), (e): comparison between the average time series of vertical displacement of the measurement points indicated in (a) (black line) and the storage curve of the UGS field (red line). The red circle in the K map indicate the location of the GNSS station.

Figure 16. Maps of the R (a) and K (b) parameters in the Field 2 monitoring area; the solid line represents the boundary of the field. (c), (d), (e): comparison between the average time series of vertical displacement of the measurement points indicated in (a) (black line) and the storage curve of the UGS field (red line).

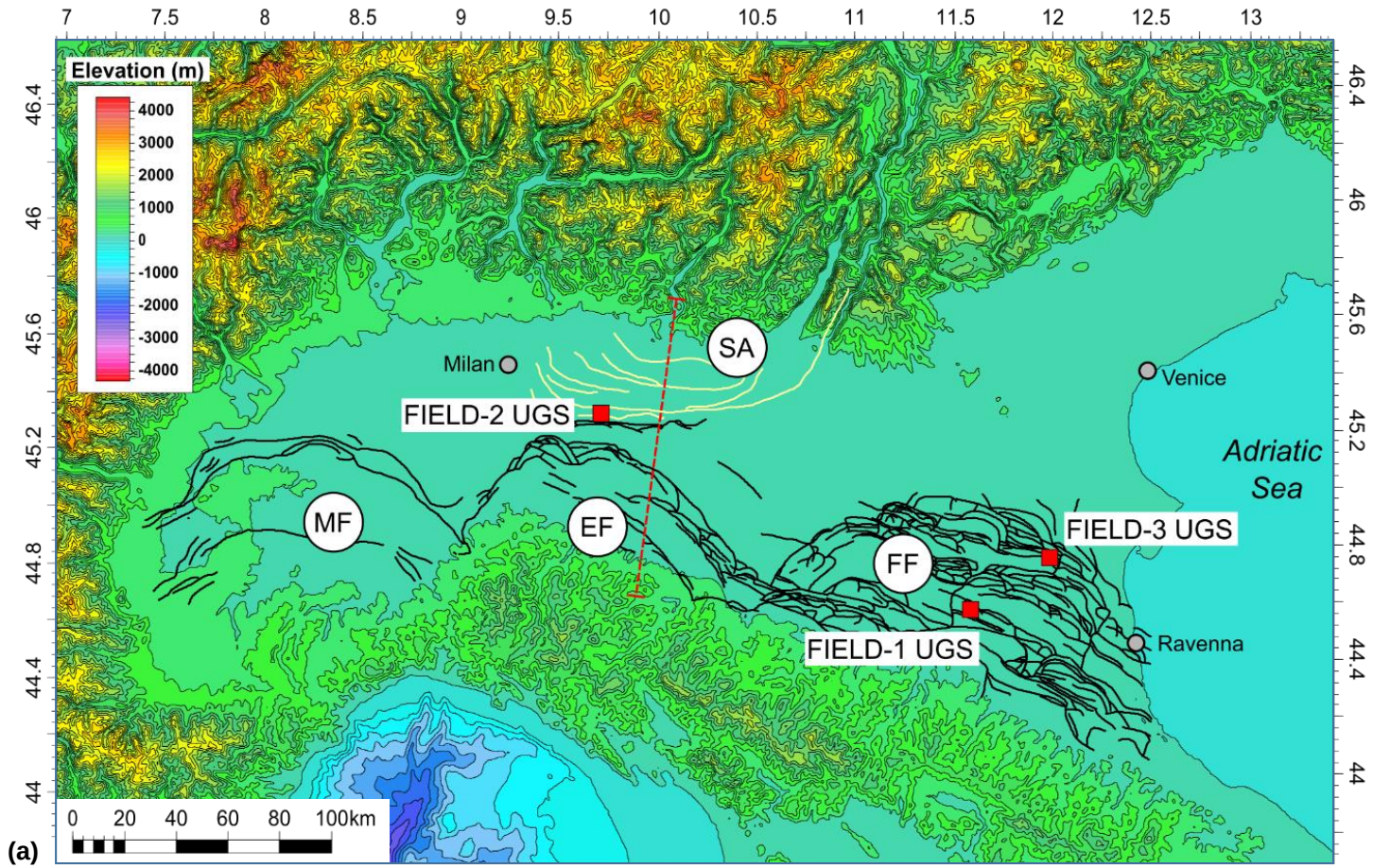
Figure 17. Maps of the R (a) and K (b) parameters in the Field 3 monitoring area; the solid line represents the boundary of the field. (c), (d), (e): comparison between the average time series of vertical displacement of the measurement points indicated in (a) (black line) and the storage curve of the UGS field (red line).

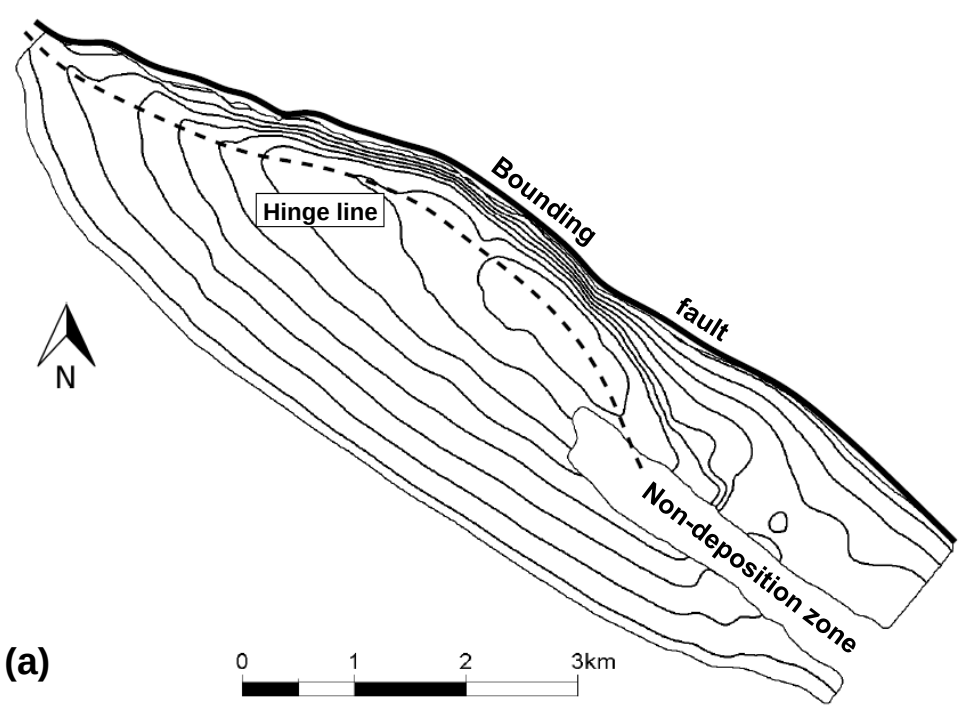
Figure 18. Distribution of the MPs with R≥0.9 compared with the structural map of the Field 1, 2, 3. The MPs are concentrated above the crest of the anticline hinge line (where most of the storage wells intersect the reservoirs); the position of the MPs reflects the degree of structural asymmetry of the buried trap.

Table 1. InSAR dataset used for the present study.

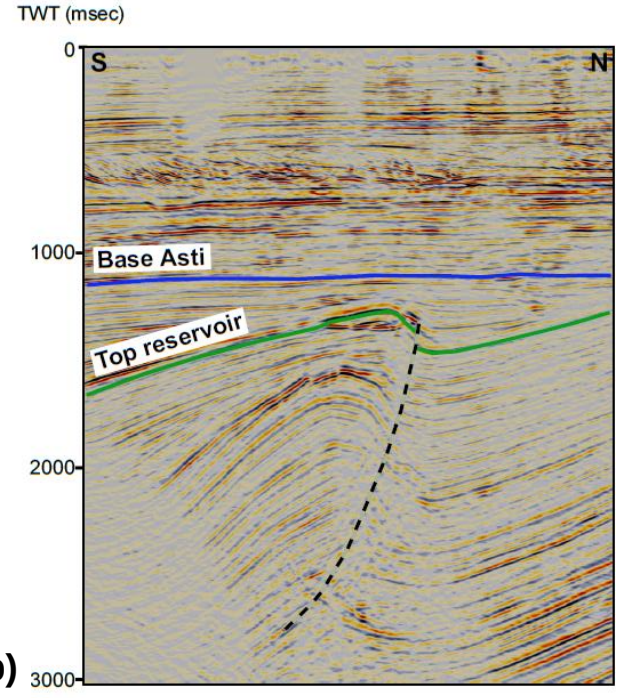
Table 2. Number of InSAR measurement points in the analyzed decomposed dataset.

Table 3. Threshold values defined for the R and K [mm/km^3] parameters.

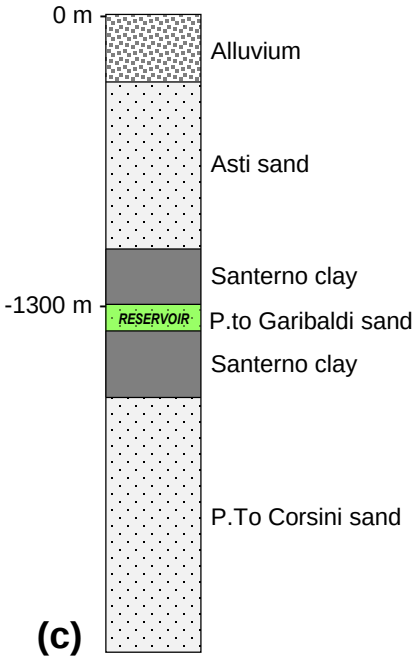

Elevation (m)
4000
3000
2000
1000
0
-1000
-2000
-3000
-4000
Milan
Venice
SA
FIELD-2 UGS
Adriatic Sea
MF
EF
FF
FIELD-3 UGS
FIELD-1 UGS
Ravenna
0 20 40 60 80 100km
7 7.5 8 8.5 9 9.5 10 10.5 11 11.5 12 12.5 13
46.4 46 45.6 45.2 44.8 44.4 44
(a)
S
N
Po plain
Northern Apennines
Southern Alps
Outcrop chain
Outcrop chain
buried front
buried front
FIELD 1
FIELD 3
FIELD 2
Pleistocene-Holocene
Mid-Late Pliocene
Eocene-Early Pliocene
Undifferentiated substratum
(b)


Hinge line
Bounding
fault
Non-deposition zone
N
0
1
2
3km

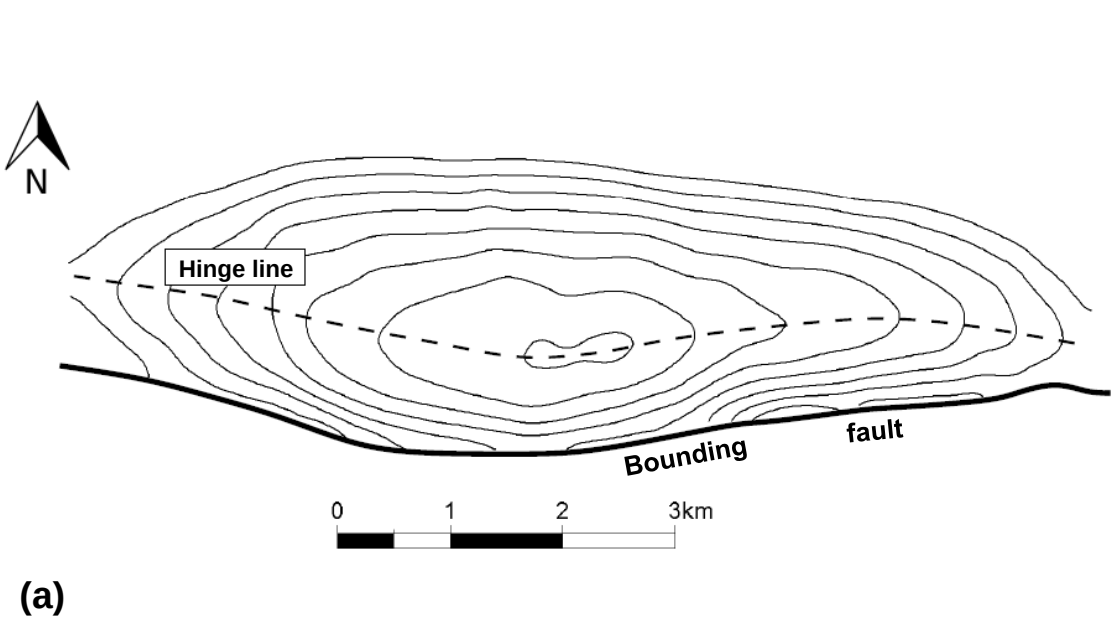
(a)


TWT (msec)
0
1000
2000
3000
S
N
Base Asti
Top reservoir

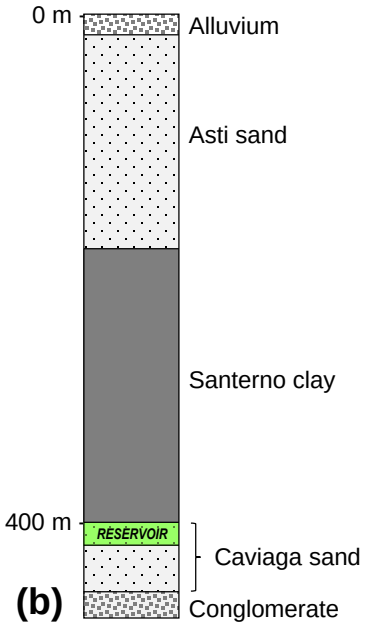
(b)


0 m
-1300 m
Alluvium
Asti sand
Santerno clay
RESERVOIR
P.to Garibaldi sand
Santerno clay
P.To Corsini sand

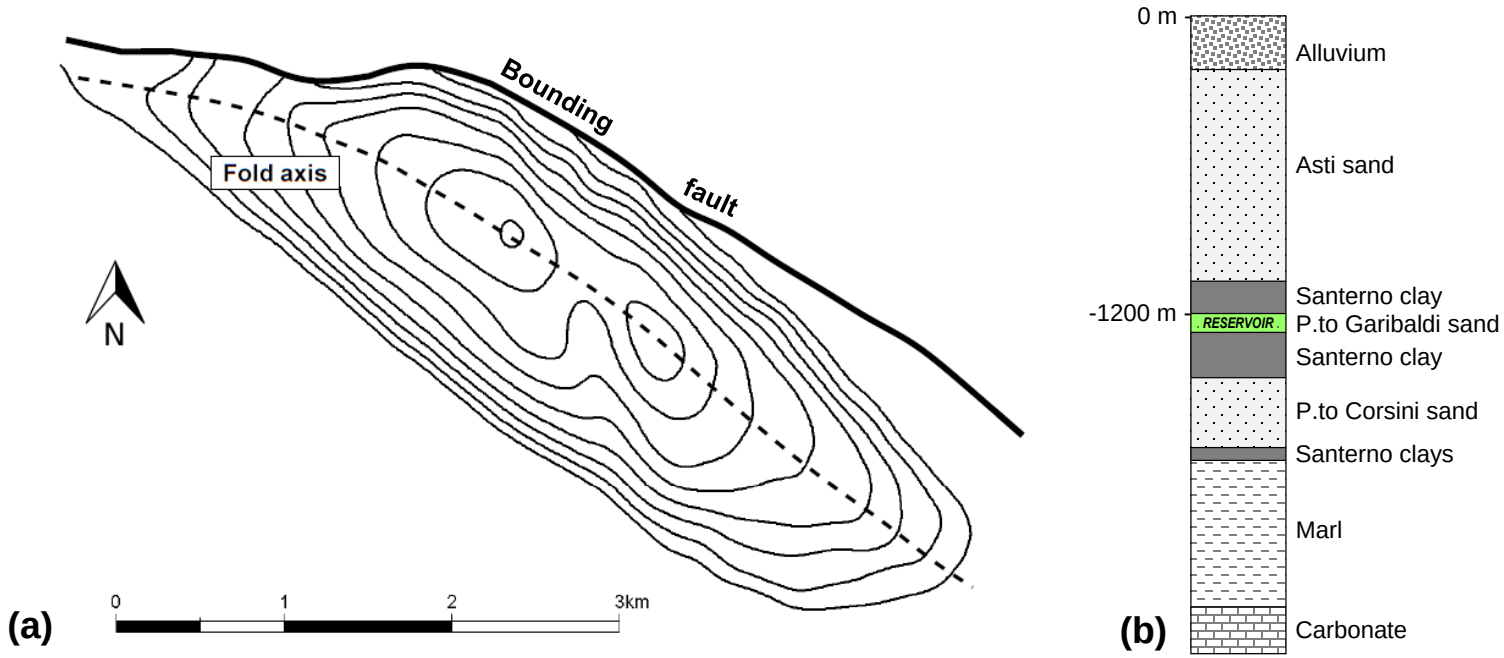
(c)

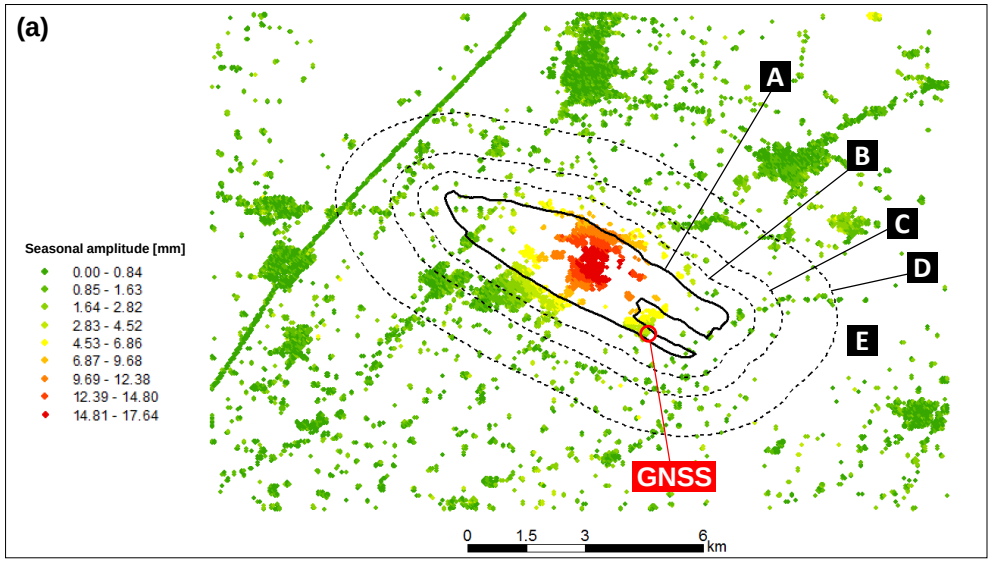

N
Hinge line
Bounding fault
0
1
2
3km

(a)


0 m
Alluvium
Asti sand
Santerno clay
400 m
RESERVOIR
Caviaga sand
Conglomerate

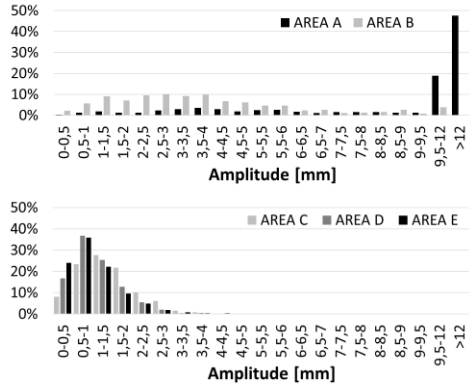
(b)

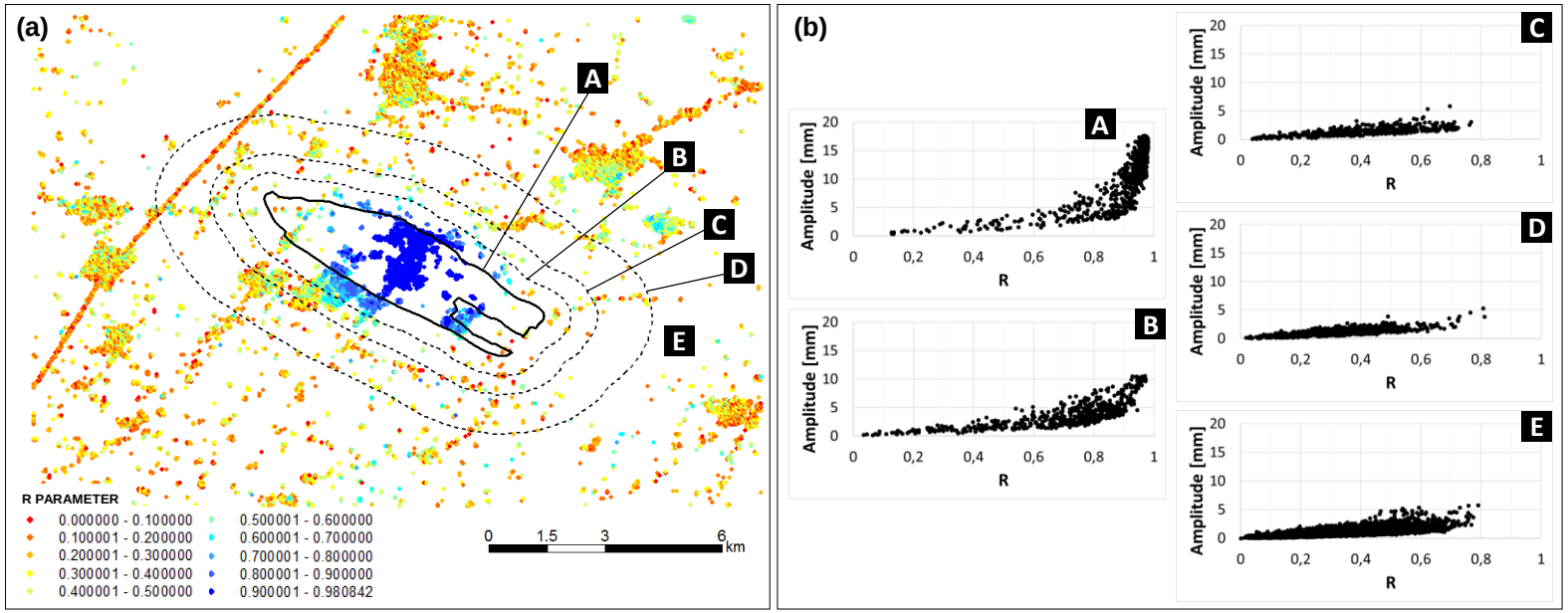

Bounding
fault
Fold axis
N
0
1
2
3km
(a)
0 m
Alluvium
Asti sand
Santerno clay
-1200 m
. RESERVOIR .
P.to Garibaldi sand
Santerno clay
P.to Corsini sand
Santerno clays
Marl
Carbonate
(b)

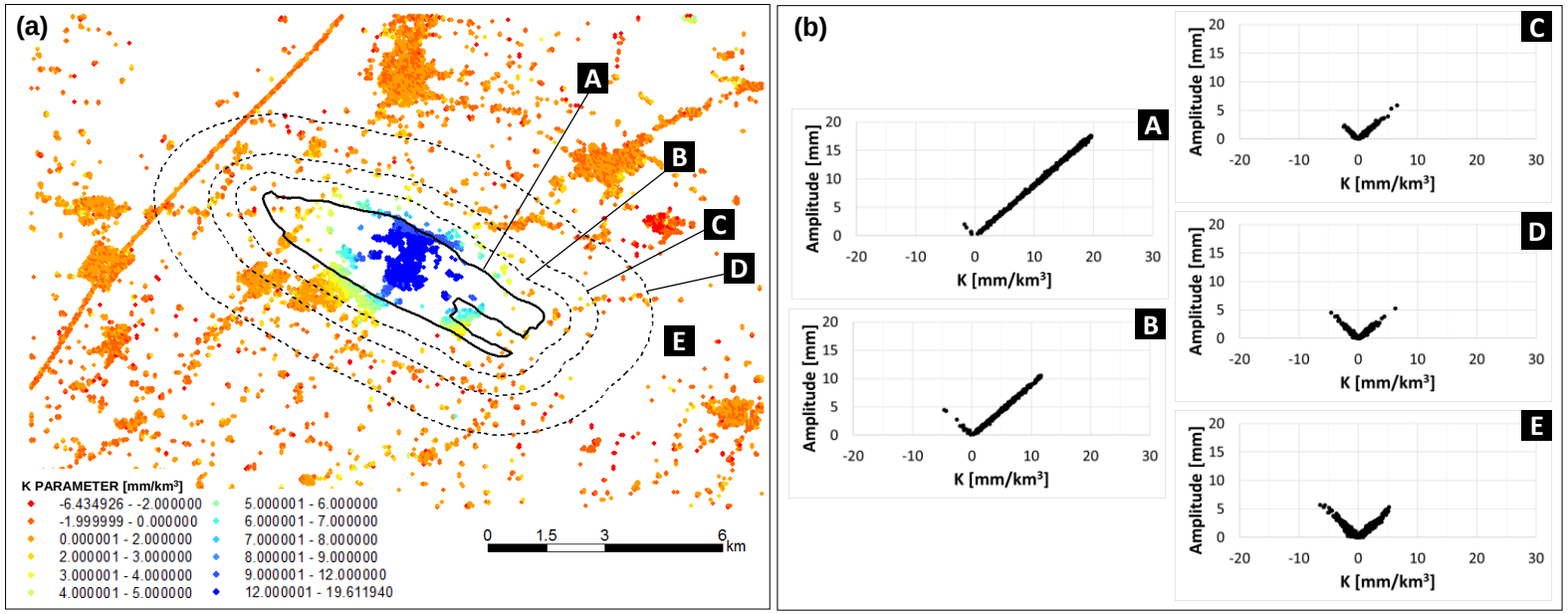


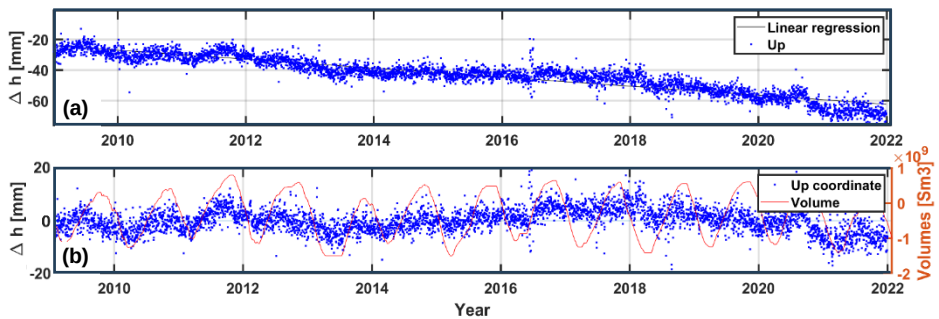
(b)

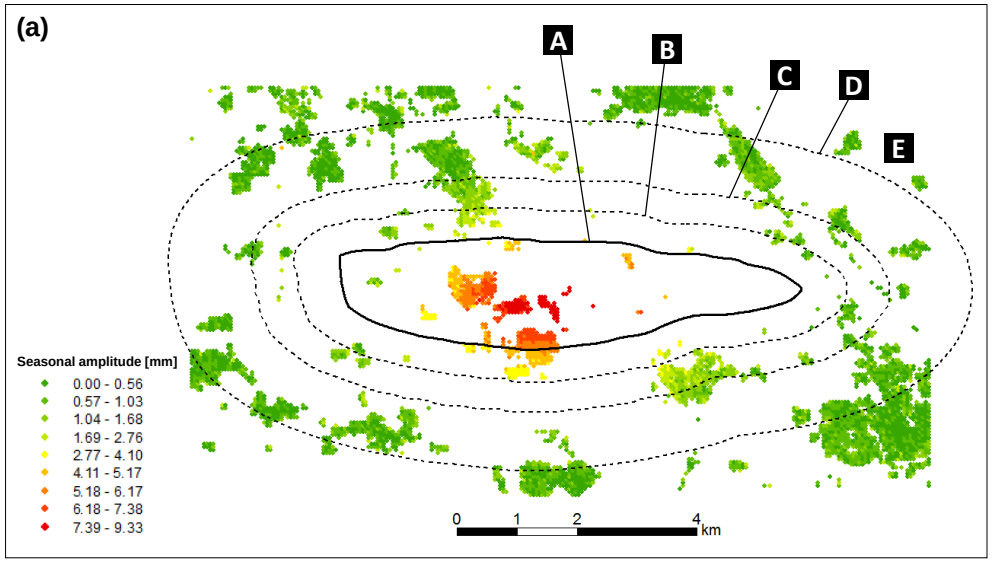
Sub-areas	Min	Max	Aver	St dev
A	0.4	17.6	**10.6**	4.7
B	0.1	10.5	**3.8**	2.4
C	0.1	5.9	**1.4**	0.7
D	0.0	5.3	**1.1**	0.6
E	0.0	5.7	**1.0**	0.7




(a)
A
B
C
D
E
R PARAMETER
0.000000 - 0.100000
0.100001 - 0.200000
0.200001 - 0.300000
0.300001 - 0.400000
0.400001 - 0.500000
0.500001 - 0.600000
0.600001 - 0.700000
0.700001 - 0.800000
0.800001 - 0.900000
0.900001 - 0.980842
0 1.5 3 6 km
(b)
Amplitude [mm]
R
0 0,2 0,4 0,6 0,8 1
0 5 10 15 20

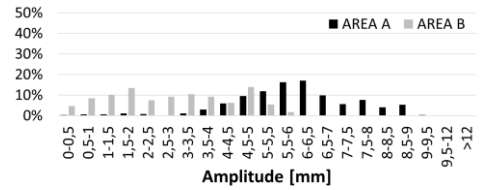

(a)
A
B
C
D
E
K PARAMETER [mm/km³]
-6.434926 - -2.000000
-1.999999 - 0.000000
0.000001 - 2.000000
2.000001 - 3.000000
3.000001 - 4.000000
4.000001 - 5.000000
5.000001 - 6.000000
6.000001 - 7.000000
7.000001 - 8.000000
8.000001 - 9.000000
9.000001 - 12.000000
12.000001 - 19.611940
0 1.5 3 6 km
(b)
A
B
C
D
E
Amplitude [mm]
K [mm/km³]

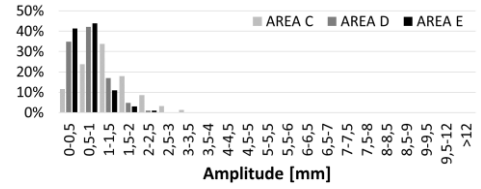

Linear regression
Up
Δ h [mm]
-20
-40
-60
(a)
2010
2012
2014
2016
2018
2020
2022
Up coordinate
Volume
Δ h [mm]
20
0
-20
(b)
×10^9
1
0
-1
-2
Volumes [Sm3]
Year

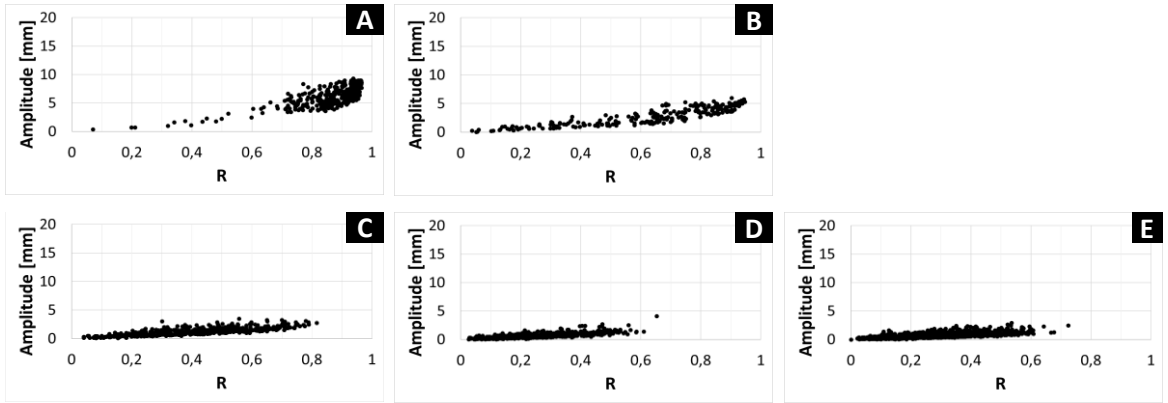


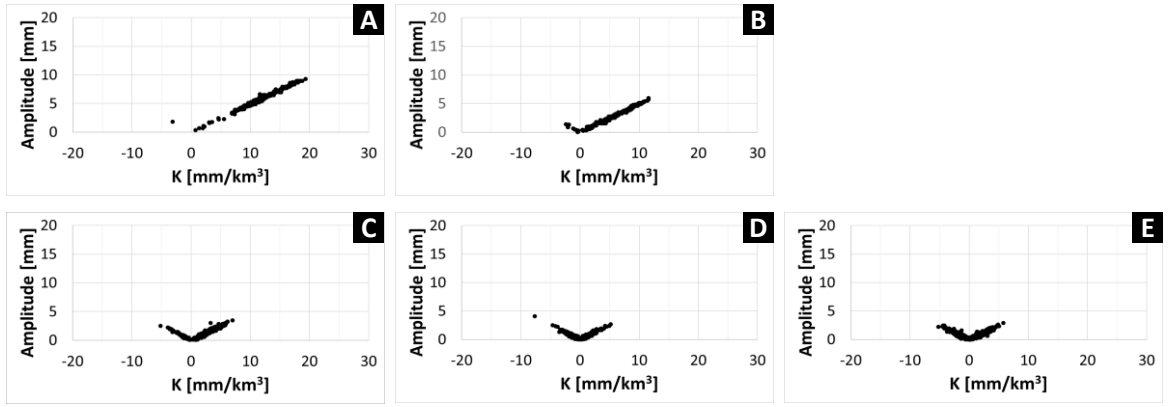
(b)

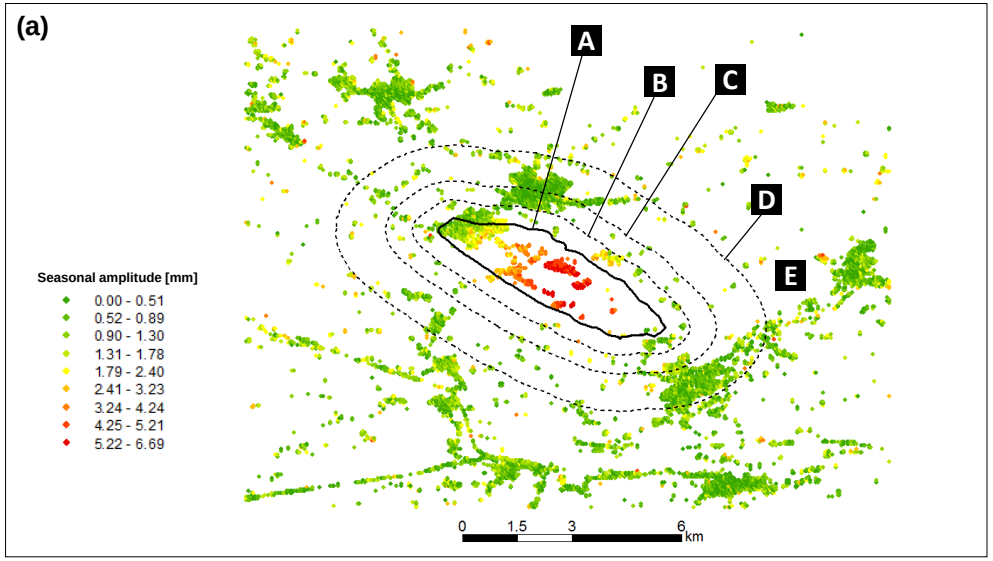
Sub-areas	Min	Max	Aver	St dev
A	0.4	9.3	**6.0**	1.5
B	0.0	5.9	**2.8**	1.5
C	0.1	3.5	**1.3**	0.6
D	0.0	4.4	**0.7**	0.5
E	0.0	2.9	**0.7**	0.4





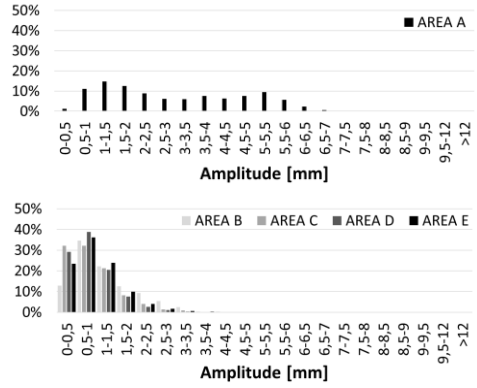

A
B
C
D
E
Amplitude [mm]
R
0
5
10
15
20
0,2
0,4
0,6
0,8
1

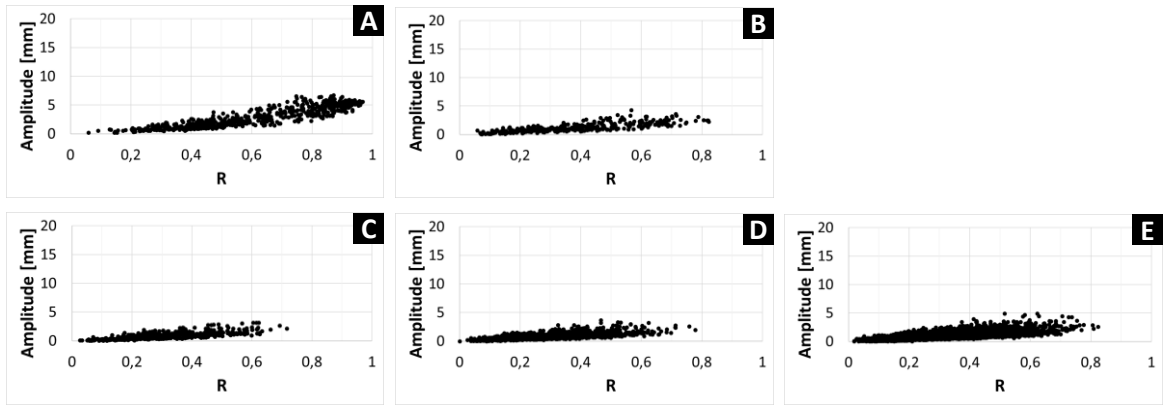

A
B
C
D
E
Amplitude [mm]
K [mm/km³]
20
15
10
5
0
-20
-10
0
10
20
30

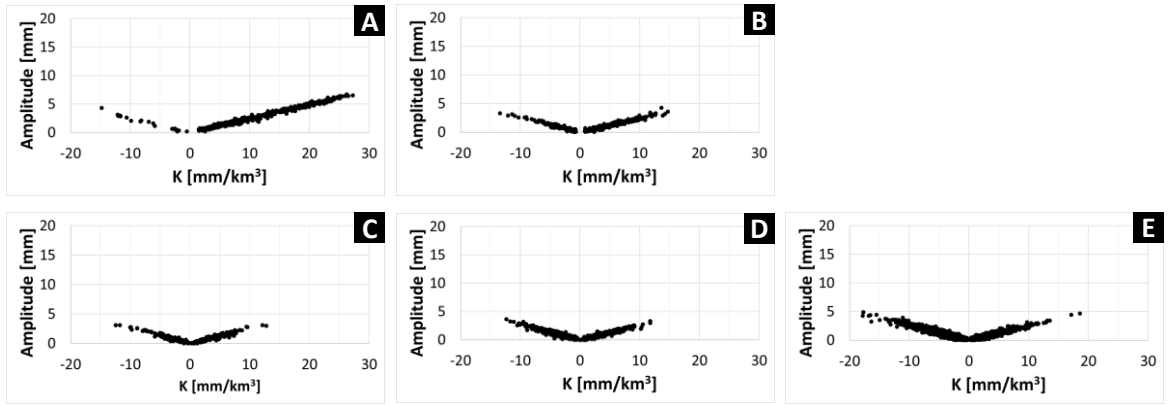


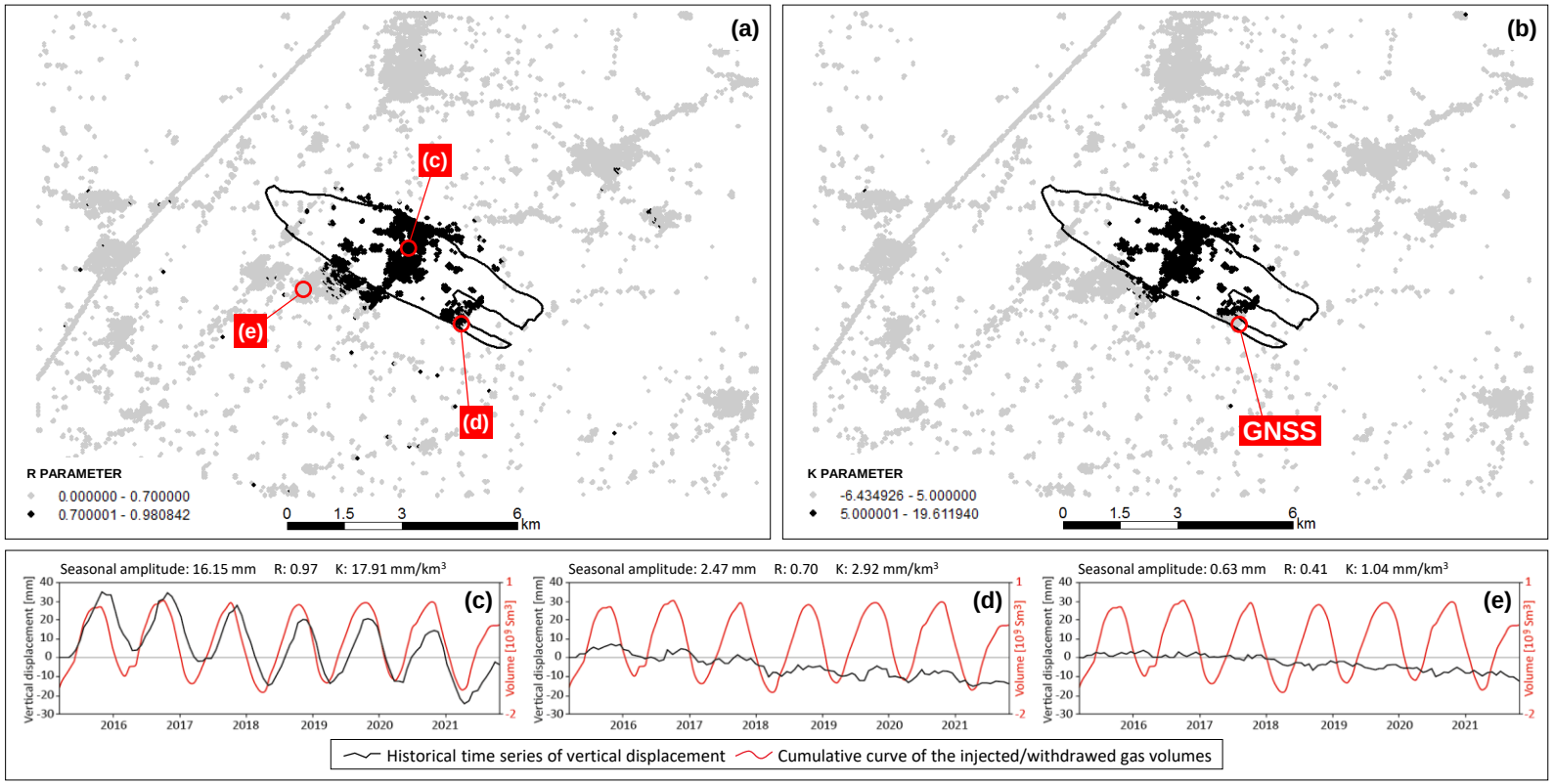
(b)

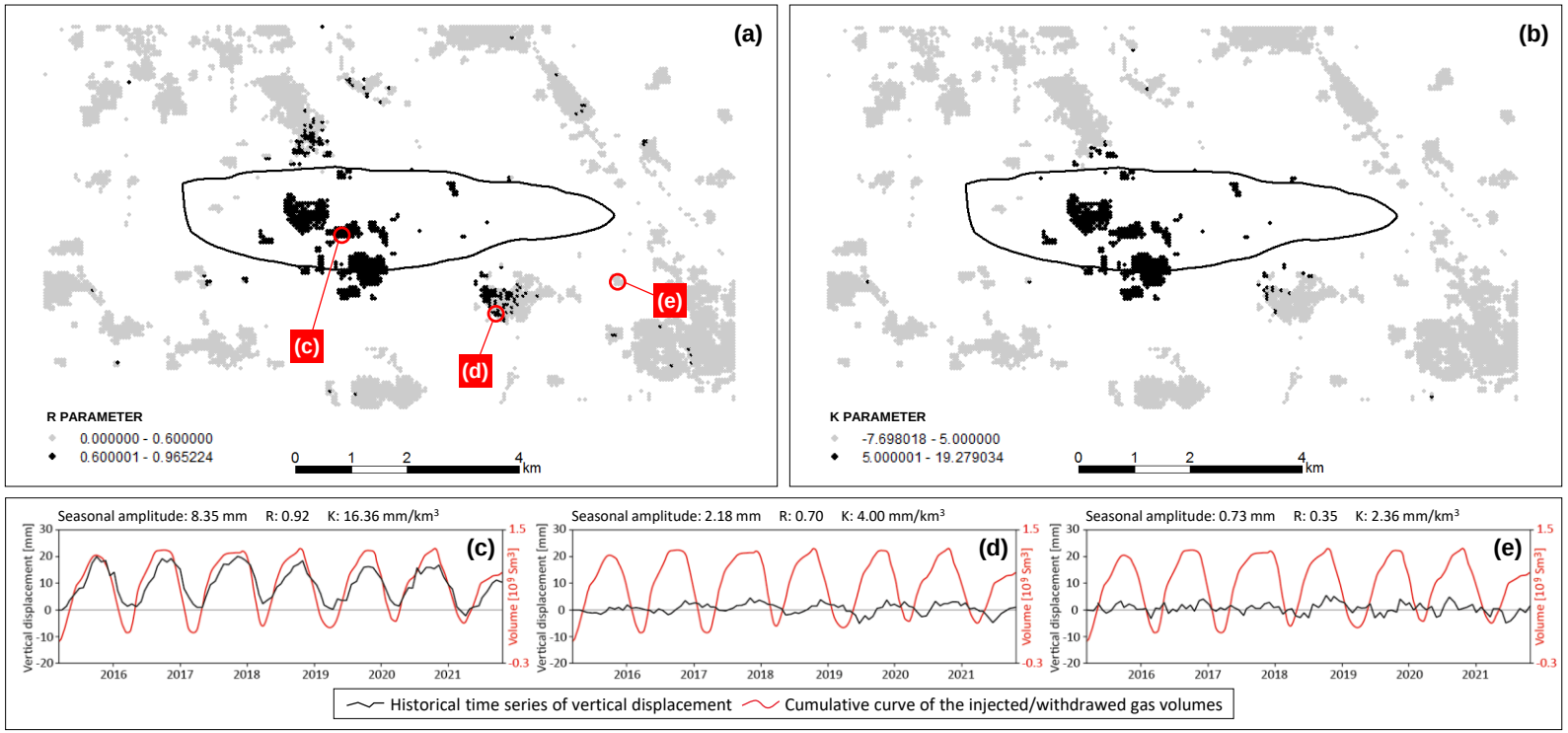
Sub-areas	Min	Max	Aver	St dev
A	0.2	6.7	**3.0**	1.7
B	0.0	4.3	**1.2**	0.8
C	0.0	3.1	**0.9**	0.6
D	0.0	3.6	**0.9**	0.5
E	0.0	4.9	**1.0**	0.6

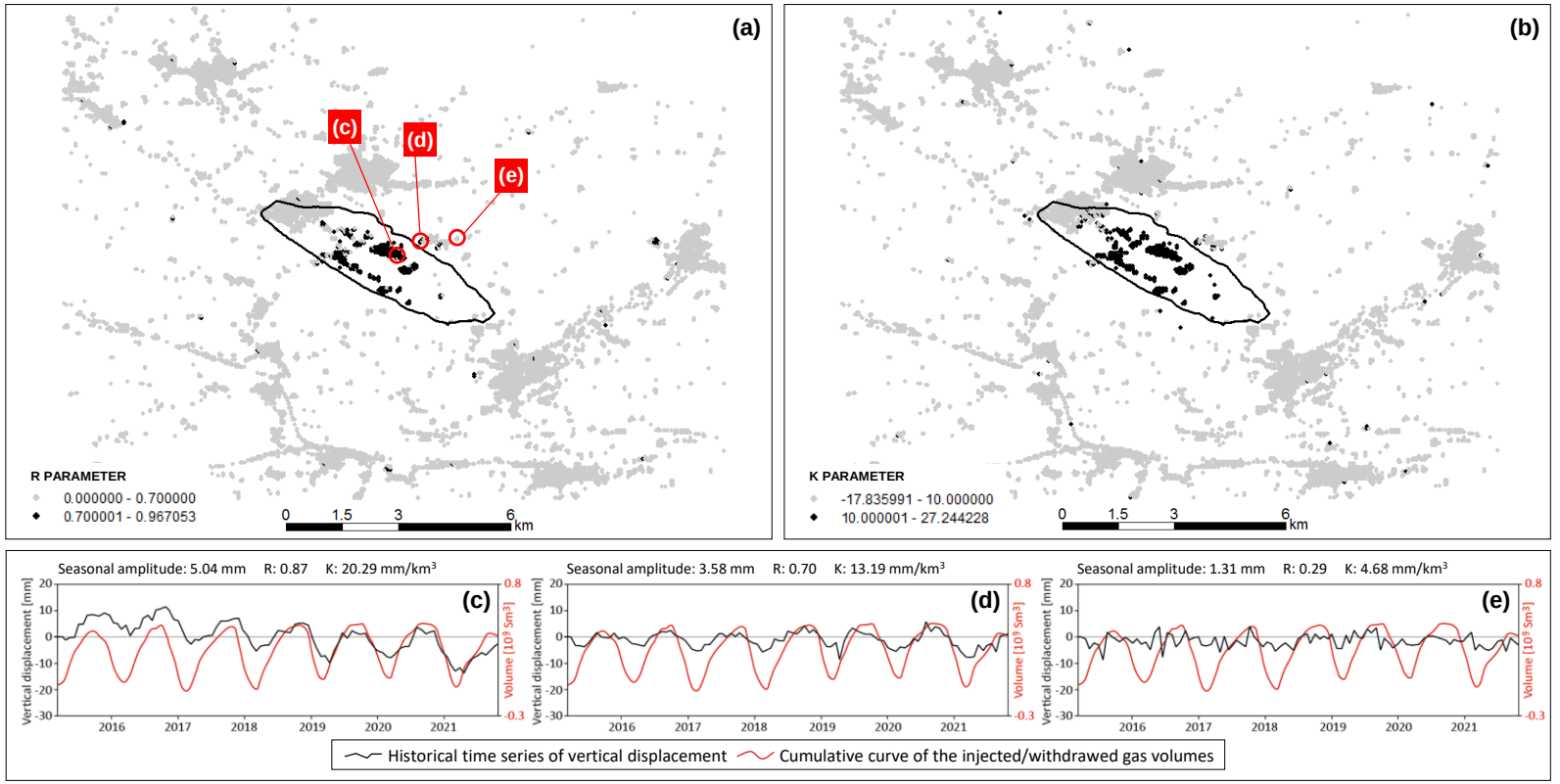


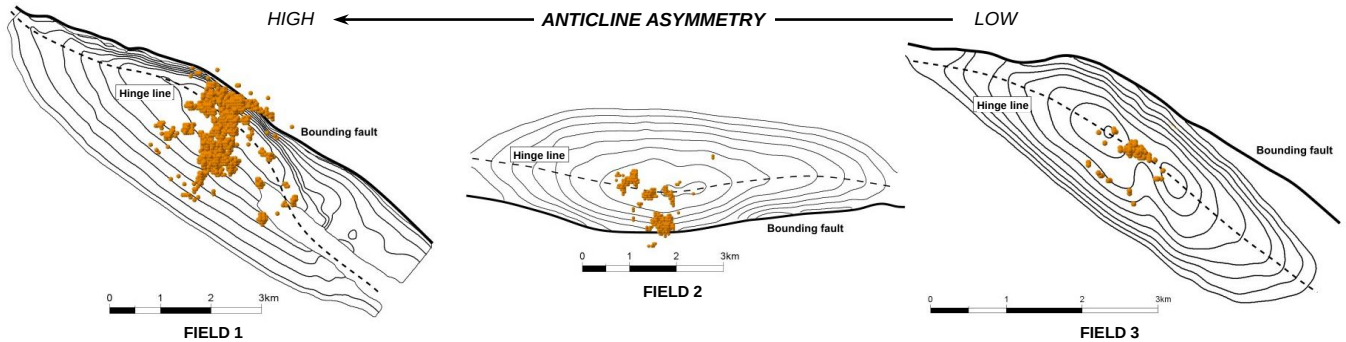

A
B
C
D
E
Amplitude [mm]
R
0
5
10
15
20
0,2
0,4
0,6
0,8
1


A
B
C
D
E
Amplitude [mm]
K [mm/km³]
20
15
10
5
0
-20
-10
0
10
20
30


(a)
(c)
(e)
(d)
R PARAMETER
0.000000 - 0.700000
0.700001 - 0.980842
0 1.5 3 6 km
(b)
GNSS
K PARAMETER
-6.434926 - 5.000000
5.000001 - 19.611940
0 1.5 3 6 km
Seasonal amplitude: 16.15 mm R: 0.97 K: 17.91 mm/km³
(c)
Seasonal amplitude: 2.47 mm R: 0.70 K: 2.92 mm/km³
(d)
Seasonal amplitude: 0.63 mm R: 0.41 K: 1.04 mm/km³
(e)
Vertical displacement [mm]
Volume [10⁹ Sm³]
2016 2017 2018 2019 2020 2021
Historical time series of vertical displacement
Cumulative curve of the injected/withdrawed gas volumes


(a)
(b)
(c)
(d)
(e)
R PARAMETER
0.000000 - 0.600000
0.600001 - 0.965224
K PARAMETER
-7.698018 - 5.000000
5.000001 - 19.279034
0 1 2 4 km
Seasonal amplitude: 8.35 mm R: 0.92 K: 16.36 mm/km³
Seasonal amplitude: 2.18 mm R: 0.70 K: 4.00 mm/km³
Seasonal amplitude: 0.73 mm R: 0.35 K: 2.36 mm/km³
Vertical displacement [mm]
Volume [10⁹ Sm³]
2016 2017 2018 2019 2020 2021
Historical time series of vertical displacement
Cumulative curve of the injected/withdrawed gas volumes


(a)
(c)
(d)
(e)
R PARAMETER
0.000000 - 0.700000
0.700001 - 0.967053
0 1.5 3 6 km
(b)
K PARAMETER
-17.835991 - 10.000000
10.000001 - 27.244228
0 1.5 3 6 km
Seasonal amplitude: 5.04 mm R: 0.87 K: 20.29 mm/km³
Seasonal amplitude: 3.58 mm R: 0.70 K: 13.19 mm/km³
Seasonal amplitude: 1.31 mm R: 0.29 K: 4.68 mm/km³
Vertical displacement [mm]
Volume [10⁹ Sm³]
2016 2017 2018 2019 2020 2021
Historical time series of vertical displacement
Cumulative curve of the injected/withdrawed gas volumes


HIGH
ANTICLINE ASYMMETRY
LOW
Hinge line
Bounding fault
0 1 2 3km
FIELD 1
Hinge line
Bounding fault
0 1 2 3km
FIELD 2
Hinge line
Bounding fault
0 1 2 3km
FIELD 3